Monthly Notices
of the
ROYAL ASTRONOMICAL SOCIETY

Mon. Not. R. Astron. Soc. **420,** 3469–3489 (2012) doi:10.1111/j.1365-2966.2011.20279.x

Modelling large-scale halo bias using the bispectrum

Jennifer E. Pollack,[1⋆] Robert E. Smith[1,2⋆] and Cristiano Porciani[1⋆]

[1]*Argelander Institut für Astronomie der Universität Bonn, Auf dem Hügel 71, D-53121 Bonn, Germany*
[2]*Institute for Theoretical Physics, University of Zurich, Zurich, CH 8037, Switzerland*

Accepted 2011 November 25. Received 2011 November 11; in original form 2011 September 14

ABSTRACT

We study the relation between the density distribution of tracers for large-scale structure and the underlying matter distribution – commonly termed bias – in the Λ cold dark matter framework. In particular, we examine the validity of the local model of biasing at quadratic order in the matter density. This model is characterized by parameters b_1 and b_2. Using an ensemble of N-body simulations, we apply several statistical methods to estimate the parameters. We measure halo and matter fluctuations smoothed on various scales. We find that, whilst the fits are reasonably good, the parameters vary with smoothing scale. We argue that, for real-space measurements, owing to the mixing of wavemodes, no smoothing scale can be found for which the parameters are independent of smoothing. However, this is not the case in Fourier space. We measure halo and halo–mass power spectra and from these construct estimates of the effective large-scale bias as a guide for b_1. We measure the configuration dependence of the halo bispectra $B_{\rm hhh}$ and reduced bispectra $Q_{\rm hhh}$ for very large-scale k-space triangles. From these data, we constrain b_1 and b_2, taking into account the full bispectrum covariance matrix. Using the lowest order perturbation theory, we find that for $B_{\rm hhh}$ the best-fitting parameters are in reasonable agreement with one another as the triangle scale is varied, although the fits become poor as smaller scales are included. The same is true for $Q_{\rm hhh}$. The best-fitting values were found to depend on the discreteness correction. This led us to consider halo–mass cross-bispectra. The results from these statistics supported our earlier findings. We then developed a test to explore whether the inconsistency in the recovered bias parameters could be attributed to missing higher order corrections in the models. We prove that low-order expansions are not sufficiently accurate to model the data, even on scales $k_1 \sim 0.04\,h\,{\rm Mpc}^{-1}$. If robust inferences concerning bias are to be drawn from future galaxy surveys, then accurate models for the full non-linear bispectrum and trispectrum will be essential.

Key words: cosmology: theory – large-scale structure of Universe.

1 INTRODUCTION

The accurate estimation and modelling of higher order clustering statistics in current and future galaxy redshift surveys has the potential to act as a powerful probe for cosmological physics. The higher order connected moments, beginning at lowest order with the three-point correlation function and its Fourier analogue, the bispectrum, when interpreted within the gravitational instability paradigm, encode important information regarding the growth of large-scale structure (Matarrese, Verde & Heavens 1997; Scoccimarro et al. 1998). Their measurements also provide insight into the statistical nature of the primordial fluctuations (Fry & Scherrer 1994; Sefusatti & Komatsu 2007; Nishimichi et al. 2010; Baldauf, Seljak & Senatore 2011) and the cosmological parameters (Sefusatti et al. 2006). Another attribute of three-point statistics, and the focus of our study, is their capability to probe the manner in which an observable tracer population of objects, such as galaxies, are related to the unobservable matter distribution – termed the 'bias' (Kaiser 1984; Dekel & Rees 1987; Fry & Gaztanaga 1993; Dekel & Lahav 1999; Catelan, Porciani & Kamionkowski 2000).

If the primordial fluctuations were Gaussian, as appears to be the case (Komatsu et al. 2011), then the statistical properties of the initial fields are fully characterized by the power spectrum, with all higher order connected correlators vanishing. However, gravitational instability leads to the coupling of Fourier modes and this generates a hierarchy of non-vanishing connected correlators, each of which has a precise characteristic mathematical structure. The matter bispectrum is thus an inherently non-linear quantity, whose signal depends on closed triangles in Fourier space. In theory, this should vanish at early times and on scales large enough where

⋆E-mail: jpollack@astro.uni-bonn.de (JEP); res@physik.unizh.ch (RES); porciani@astro.uni-bonn.de (CP)

linear theory is valid. If galaxy bias is local and linear, then the bispectrum of the observable tracers is proportional to the matter bispectrum. If, on the other hand, bias is local and non-linear, then the triangle configuration dependence of the signal is modified, and this happens in a very precise and calculable way. Thus, the bispectrum can be used to constrain the bias (Fry & Gaztanaga 1993; Matarrese, Verde & Heavens 1997; Scoccimarro, Couchman & Frieman 1999).

There is a long and rich history of measurements of three-point statistics from galaxy surveys, going all the way back to Peebles & Groth (1975). However, attempts to constrain the non-linearity of galaxy bias from galaxy redshift surveys have only been performed over the last decade. Feldman et al. (2001) and Scoccimarro et al. (2001a) both analysed *IRAS* survey using the bispectrum, and found a negative quadratic bias, although due to small sample size the constraints were rather weak. Verde et al. (2002) analysed 2dFGRS, also using the bispectrum approach, and claimed that the flux-limited sample was an unbiased tracer of the dark matter. A subsequent analysis of the final 2dFGRS data set by Gaztañaga et al. (2005), using the three-point correlation function, contradicted this: using information from weakly-non-linear scales ($R \sim 6$–$27\,h^{-1}$ Mpc), the unbiased case ($b_1 = 1$ and $b_2 = 0$) was excluded at the order of 9σ. More recently a number of authors have analysed various data releases of SDSS (Nishimichi et al. 2007 – Third Data Release; McBride et al. 2011 – Sixth Data Release; Marin 2011 – Seventh Data Release). These all claim a non-zero quadratic bias term for most of the samples within the data set. Obviously, these variations of the results with survey and statistical method require an explanation.

Whilst the local bias model can be used to test whether the bias is linear or non-linear, a significant detection of non-zero non-linear bias does not imply that we have understood the bias. In order to believe that these measurements are meaningful, we need to be sure that the local model is indeed the correct model for interpreting data. This is currently an open question. Attempting to shed light on this subject is one of the aims of this paper. Over the past few years, the local model of galaxy bias has been scrutinized by a number of authors (Heavens, Matarrese & Verde 1998; Gaztañaga & Scoccimarro 2005; Smith, Scoccimarro & Sheth 2007; Guo & Jing 2009; Manera, Sheth & Scoccimarro 2010; Manera & Gaztañaga 2011; Roth & Porciani 2011). However, no firm conclusions have yet been reached.

In this paper, we use a large ensemble of 40 mid-resolution, large-volume, pure dark matter N-body simulations to test the validity of the local bias model. In this study, we compare a selection of different methods for determining the bias. We first present a point-wise comparison of the halo and matter density fields smoothed on certain scales. We also utilize the power spectrum to estimate a large-scale effective bias parameter. Then we expend most of our efforts on using the bispectrum and reduced bispectrum approaches for constraining the bias. Besides the auto-bispectra, we also present, for the first time, measurements of the halo–mass cross-bispectra: $B_{\rm hhm}$ and $B_{\rm hmm}$, and $Q_{\rm hhm}$ and $Q_{\rm hmm}$. The value of these new statistics becomes apparent when correcting for shot-noise effects. Finally, we perform a numerical test that allows us to sharply illuminate the importance of terms in the theory that are beyond the tree-level expansions typically used.

The layout of this paper is as follows. In Section 2, we present the theory for the matter bispectrum and the local bias model. In Section 3, we provide details of the numerical simulations used in this work. In Section 4, we present the results for the bias parameters from the various commonly used simple estimators. In Section 5, we present the estimation of the bias from the bispectrum. Then, in Section 6, we present measurements of bias from the cross-bispectra. In Section 7, we present a test of the importance of terms in the theory that are beyond tree level. Finally, in Sections 8 and 9, we discuss our findings and present our conclusions.

2 THEORETICAL OVERVIEW

2.1 Standard perturbation theory dynamics

In the fluid approximation, the gravitational collapse of collisionless cold matter structures in the expanding Universe can be fully characterized by specifying the evolution of the density $\delta\rho(\boldsymbol{x})$ and the peculiar velocity $\delta\boldsymbol{v}(\boldsymbol{x})$ perturbations (Bernardeau et al. 2002). Focusing primarily on the density field, we work with models of the matter density contrast:

$$\delta(\boldsymbol{x},t) \equiv \frac{\rho(\boldsymbol{x},t)-\overline{\rho}(t)}{\overline{\rho}(t)}, \tag{1}$$

where $\bar{\rho}(t)$ is the mean matter density of the Universe. In Fourier space, we define its corresponding Fourier representation, $\delta(\boldsymbol{k})$, accordingly, as

$$\delta(\boldsymbol{x}) = \int \frac{\mathrm{d}^3\boldsymbol{k}}{(2\pi)^3}\delta(\boldsymbol{k})\mathrm{e}^{-\mathrm{i}\boldsymbol{k}\cdot\boldsymbol{x}} \quad \Leftrightarrow \quad \delta(\boldsymbol{k}) = \int \mathrm{d}^3\boldsymbol{x}\,\delta(\boldsymbol{x})\mathrm{e}^{\mathrm{i}\boldsymbol{k}\cdot\boldsymbol{x}}. \tag{2}$$

It can be shown that the non-linear equations of motion for $\delta(\boldsymbol{k})$ can be solved exactly by perturbative expansions of the type (Juszkiewicz 1981; Vishniac 1983; Goroff et al. 1986)

$$\delta(\boldsymbol{k}) = \sum_{n=1}^{\infty} a^n(t)\delta_n(\boldsymbol{k}), \tag{3}$$

where $\delta_n(\boldsymbol{k})$ is given by

$$\delta_n(\boldsymbol{k}) = \int \frac{\mathrm{d}^3\boldsymbol{q}_1}{(2\pi)^3}\cdots\int \frac{\mathrm{d}^3\boldsymbol{q}_n}{(2\pi)^3}\,(2\pi)^3\delta^{\rm D}(\boldsymbol{k}-\boldsymbol{q}_1-\cdots-\boldsymbol{q}_n) \times F_n(\boldsymbol{q}_1,\ldots,\boldsymbol{q}_n)\delta_1(\boldsymbol{q}_1)\cdots\delta_1(\boldsymbol{q}_n)\,. \tag{4}$$

The density kernel F_n is the dimensionless, homogeneous, mode-coupling function that couples together the amplitudes and phases of n initial Fourier wavemodes $\{\delta(\boldsymbol{q}_1),\ldots,\delta(\boldsymbol{q}_n)\}$. As was shown by Goroff et al. (1986), Makino et al. (1992) and Jain & Bertschinger (1994), the nth-order kernel may be constructed recursively from the lower order solutions. Linear theory is thus represented by $F_1(\boldsymbol{q}_1) = 1$, and the first non-linear correction by F_2, where

$$F_2(\boldsymbol{k}_1,\boldsymbol{k}_2) = \frac{5}{7} + \frac{\boldsymbol{k}_1\cdot\boldsymbol{k}_2}{k_1k_2}\left(\frac{k_1}{k_2}+\frac{k_2}{k_1}\right) + \frac{2}{7}\frac{(\boldsymbol{k}_1\cdot\boldsymbol{k}_2)^2}{k_1^2k_2^2}. \tag{5}$$

The above approach defines the standard perturbation theory (hereafter SPT). Before moving on, we note that the above statements are only exactly true for the Einstein–de Sitter model. However, it has been shown that the F_2 kernel is almost independent of cosmology (Fry 1994; Bouchet et al. 1995; Hivon et al. 1995). We therefore adopt equation (5) when dealing with the density at second order.

2.2 From dynamics to statistics

Owing to the stochastic nature of the density field, we are not interested in reproducing a specific density field per se, but instead in characterizing its statistical properties. In this work, we focus on two- and three-point correlation functions in Fourier space. These we may write as

$$\langle\delta(\boldsymbol{k}_1)\delta(\boldsymbol{k}_2)\rangle \equiv (2\pi)^3\,\delta^{\rm D}(\boldsymbol{k}_{12})P_{\rm mm}(k_1), \tag{6}$$

$$\langle\delta(\boldsymbol{k}_1)\delta(\boldsymbol{k}_2)\delta(\boldsymbol{k}_3)\rangle \equiv (2\pi)^3\,\delta^{\rm D}(\boldsymbol{k}_{123})B_{\rm mmm}(\boldsymbol{k}_1,\boldsymbol{k}_2,\boldsymbol{k}_3), \tag{7}$$

where $P_{\rm mm}(k)$ and $B_{\rm mmm}(\boldsymbol{k}_1,\boldsymbol{k}_2,\boldsymbol{k}_3)$ constitute definitions of the power and bispectrum. For the Dirac delta functions, we used the short-hand notation $\delta^{\rm D}(\boldsymbol{k}_{1\ldots n}) \equiv \delta^{\rm D}(\boldsymbol{k}_1+\cdots+\boldsymbol{k}_n)$ and these guarantee that P and B are translationally invariant. This is an important property for estimation, since it means that we should consider only closed pairs and triangles in Fourier space: $\sum \boldsymbol{k}_i = 0$.

The perturbative expansion of the density field described in the previous section implies that $P_{\rm mm}$ and $B_{\rm mmm}$ may also be described in a perturbative fashion. Hence,

$$\langle\delta(\boldsymbol{k}_1)\delta(\boldsymbol{k}_2)\rangle = \langle[\delta_1(\boldsymbol{k}_1)+\delta_2(\boldsymbol{k}_1)+\cdots] \times [\delta_1(\boldsymbol{k}_2)+\delta_2(\boldsymbol{k}_2)+\cdots]\rangle\ , \tag{8}$$

$$\langle\delta(\boldsymbol{k}_1)\ldots\delta(\boldsymbol{k}_3)\rangle = \langle[\delta_1(\boldsymbol{k}_1)+\delta_2(\boldsymbol{k}_1)+\cdots]\cdots \times [\delta_1(\boldsymbol{k}_3)+\delta_2(\boldsymbol{k}_3)+\cdots]\rangle\,. \tag{9}$$

Since we are assuming that the initial Fourier modes are Gaussianly distributed, that is, the phase of each initial mode is uniformly random $\phi \in [0, 2\pi]$, modes must cancel in pair. Hence, Wick's theorem applies, and so odd products of initial Fourier modes must vanish: $\langle\delta_1(\boldsymbol{k}_1)\delta_2(\boldsymbol{k}_2)\rangle = \langle\delta_1(\boldsymbol{k}_1)\delta_1(\boldsymbol{k}_2)\delta_1(\boldsymbol{k}_3)\rangle = 0$. This led us to write the perturbative expansions for $P_{\rm mm}$ and $B_{\rm mmm}$ as

$$P_{\rm mm}(k) = P^{(0)}_{\rm mm}(k) + P^{(1)}_{\rm mm}(k) + \cdots\ , \tag{10}$$

$$B_{\rm mmm}(\boldsymbol{k}_1,\boldsymbol{k}_2) = B^{(0)}_{\rm mmm}(\boldsymbol{k}_1,\boldsymbol{k}_2) + B^{(1)}_{\rm mmm}(\boldsymbol{k}_1,\boldsymbol{k}_2) + \cdots\ . \tag{11}$$

We shall refer to the lowest order terms in the expansions as 'tree-level' terms. For P, $P^{(0)}$ is simply the linear spectrum, while for B the tree-level term can be written as

$$B^{(0)}_{\rm mmm}(\boldsymbol{k}_1,\boldsymbol{k}_2) = 2\,P^{(0)}_{\rm mm}(k_1)\,P^{(0)}_{\rm mm}(k_2)\,F_2(\boldsymbol{k}_1,\boldsymbol{k}_2) + 2\ \text{cyc.} \tag{12}$$

In this work, we shall mainly be dealing with tree-level quantities; we now set $P^{(0)}_{\rm mm} = P_{\rm mm}$ and $B^{(0)}_{\rm mmm} = B_{\rm mmm}$, unless otherwise stated.

Another statistical quantity commonly used to explore galaxy clustering is the reduced bispectrum (Peebles & Groth 1975; Scoccimarro et al. 1998), which can be defined as

$$Q_{\rm mmm}(\boldsymbol{k}_1,\boldsymbol{k}_2,\boldsymbol{k}_3) \equiv \frac{B_{\rm mmm}(\boldsymbol{k}_1,\boldsymbol{k}_2,\boldsymbol{k}_3)}{P_{\rm mm}(k_1)P_{\rm mm}(k_2)+2\,\text{cyc}}. \tag{13}$$

As will be made clear below, the importance of this statistic becomes apparent when one considers non-Gaussian terms that are generated by simple quadratic products of Gaussian fields. In this case, $Q_{\rm mmm}$ simply scales as a constant.

2.3 Halo bias: local form

In this study, we investigate the relation between the clustering of dark matter haloes and total matter. If galaxies are only formed in dark matter haloes, as is the usual assumption for all models of galaxy formation (White & Rees 1978), then understanding the clustering of haloes is an essential component of any theory of galaxy biasing (Smith et al. 2007). In the local model of halo biasing, the number density of dark matter haloes of mass scale M, smoothed over a scale R, can be expressed as a function of the local matter density, smoothed on the scale R. This function may then be Taylor expanded to give (Coles 1993; Fry & Gaztanaga 1993; Mo, Jing & White 1997; Smith et al. 2007)

$$\delta_{\rm h}(\boldsymbol{x}|M,R) = \sum_{j=0}^{\infty}\frac{b_j(M)}{j!}[\delta(\boldsymbol{x}|R)]^j, \tag{14}$$

where we defined the smoothed halo overdensity to be $\delta_{\rm h}(\boldsymbol{x}|M,R) \equiv [\overline{n}_{\rm h}(\boldsymbol{x}|M,R)-\overline{n}_{\rm h}(M)]/\overline{n}_{\rm h}(M)$. Owing to the fact that $\langle\delta_{\rm h}\rangle = 0$, the constant coefficient $b_0(M) = -\sum_{j=2}^{\infty} b_j(M)\langle\delta^j\rangle/j!$ (Fry & Gaztanaga 1993). Note that on Fourier transforming $\delta_{\rm h}(\boldsymbol{x}|M,R)$ the constant b_0 only contributes to the unmeasurable $k=0$ mode. The terms $b_1(M)$ and $b_2(M)$ represent the linear and first non-linear bias parameters, respectively.

In Fourier space, equation (14) can be written as

$$\delta_{\rm h}(\boldsymbol{k}|M,R) = b_1(M)\delta(\boldsymbol{k}|R) + \frac{b_2(M)}{2}\int\frac{{\rm d}^3\boldsymbol{q}_1}{(2\pi)^3}\delta(\boldsymbol{q}_1|R)\delta(\boldsymbol{k}-\boldsymbol{q}_1|R)+\cdots, \tag{15}$$

where $\delta_i(\boldsymbol{q}_j|R) \equiv W(|\boldsymbol{q}_j|R)\delta_i(\boldsymbol{q}_j)$. If one inserts the SPT expansions for the density into the local model, then, up to second order in the density and bias, one finds

$$\delta^{\rm h}(\boldsymbol{k}|M,R) = b_1(M)\,[\delta_1(\boldsymbol{k}|R)+\delta_2(\boldsymbol{k}|R)] + \frac{b_2(M)}{2}\int\frac{{\rm d}^3\boldsymbol{q}_1}{(2\pi)^3}\delta_1(\boldsymbol{q}_1|R)\delta_1(\boldsymbol{k}-\boldsymbol{q}_1|R). \tag{16}$$

Using this approach one may then find a perturbative expansion for the halo power and bispectra:

$$P_{\rm hh}(M) = P^{(0)}_{\rm hh}(M) + P^{(1)}_{\rm hh}(M) + \cdots\ , \tag{17}$$

$$B_{\rm hhh}(M) = B^{(0)}_{\rm hhh}(M) + B^{(1)}_{\rm hhh}(M) + \cdots. \tag{18}$$

Again, we refer to the lowest order terms in these expansions as tree-level terms, and for these we have

$$\widetilde{\mathcal{P}}^{(0)}_{\rm hh}(k|M) = b_1^2(M)\widetilde{\mathcal{P}}_{\rm mm}(k)\ , \tag{19}$$

$$\widetilde{\mathcal{B}}^{(0)}_{\rm hhh}(\boldsymbol{k}_1,\boldsymbol{k}_2|M) = b_1^3(M)\widetilde{\mathcal{B}}_{\rm mmm}(\boldsymbol{k}_1,\boldsymbol{k}_2) + b_1^2(M)b_2(M) \times\left[\widetilde{\mathcal{P}}_{\rm mm}(k_1)\widetilde{\mathcal{P}}_{\rm mm}(k_2)+2\,\text{cyc}\right], \tag{20}$$

where in the above expressions we have derived the spectra of the smoothed fields: $\widetilde{\mathcal{P}} \equiv W^2(kR)P(k)$, and $\widetilde{\mathcal{B}} \equiv W(k_1R)W(k_2R)W(k_3R)B$. However, when we estimate the bispectrum from data, we do not smooth the fields apart from the 'Cloud-in-Cell' (CIC) assignment scheme used to obtain the density contrast field. As pointed out by Smith et al. (2007), Smith, Sheth & Scoccimarro (2008) and Sefusatti (2009), one way to overcome this is to adopt the ansatz

$$P^{(0)}_{\rm hh}(k|M) = \frac{\widetilde{\mathcal{P}}^{(0)}_{\rm hh}(k|M,R)}{W^2(kR)}\ , \tag{21}$$

$$B^{(0)}_{\rm hhh}(\boldsymbol{k}_1,\boldsymbol{k}_2,\boldsymbol{k}_3|M) = \frac{\widetilde{\mathcal{B}}^{(0)}_{\rm hhh}(\boldsymbol{k}_1,\boldsymbol{k}_2,\boldsymbol{k}_3|M,R)}{W(k_1R)W(k_2R)W(k_3R)}. \tag{22}$$

On applying this 'de-smoothing' operation to equations (19) and (20), one finds

$$P^{(0)}_{\rm hh}(k|M) = b_1^2(M)P_{\rm mm}(k)\ , \tag{23}$$

$$B^{(0)}_{\rm hhh}(\boldsymbol{k}_1,\boldsymbol{k}_2|M) = b_1^3(M)B_{\rm mmm}(\boldsymbol{k}_1,\boldsymbol{k}_2) + b_1^2(M)\,b_2(M) \times\widetilde{W}_{k_1,k_2}P_{\rm mm}(k_1)P_{\rm mm}(k_2)+2\,\text{cyc}\,, \tag{24}$$

where we have defined the function (Sefusatti 2009)

$$\widetilde{W}_{k_1,k_2} \equiv \frac{W(|\boldsymbol{k}_1|R)W(|\boldsymbol{k}_2|R)}{W(|\boldsymbol{k}_1+\boldsymbol{k}_2|R)}. \tag{25}$$

Note that in the limit of very large scales or arbitrarily small smoothing scales, $k_iR \to 0$ for $i \in \{1,\,2,\,3\}$, equation (24)

approximates to

$$B^{(0)}_{\rm hhh}(\boldsymbol{k}_1,\boldsymbol{k}_2|M) \approx b_1^3(M)B_{\rm mmm}(\boldsymbol{k}_1,\boldsymbol{k}_2) + b_1^2(M)\,b_2(M) \times \left[P_{\rm mm}(k_1)P_{\rm mm}(k_2) + 2\,{\rm cyc}\right]. \quad (26)$$

Again, since in this paper we are only considering tree-level expressions we shall take $P^{(0)}_{\rm hh} \to P_{\rm hh}$ and $B^{(0)}_{\rm hhh} \to B_{\rm hhh}$.

Considering now the reduced halo bispectrum, it may be defined in a similar fashion to equation (13):

$$Q_{\rm hhh}(\boldsymbol{k}_1,\boldsymbol{k}_2,\boldsymbol{k}_3|M) \equiv \frac{B_{\rm hhh}(\boldsymbol{k}_1,\boldsymbol{k}_2|M)}{P_{\rm hh}(k_1|M)P_{\rm hh}(k_2|M) + 2\,{\rm cyc}}. \quad (27)$$

On inserting our tree-level expressions from equations (23) and (24), we find that

$$Q_{\rm hhh}(M) = \frac{Q_{\rm mmm}}{b_1(M)} + \frac{b_2(M)}{b_1^2(M)}\alpha(\boldsymbol{k}_1,\boldsymbol{k}_2,\boldsymbol{k}_3), \quad (28)$$

where we have defined

$$\alpha(\boldsymbol{k}_1,\boldsymbol{k}_2,\boldsymbol{k}_3) \equiv \frac{\widetilde{W}_{k_1,k_2}P(k_1)P(k_2) + 2\,{\rm cyc}}{P(k_1)P(k_2) + 2\,{\rm cyc}}\,. \quad (29)$$

Again, in the limit of very large scales or arbitrarily small smoothing scales and $\alpha(\boldsymbol{k}_1,\boldsymbol{k}_2,\boldsymbol{k}_3) \to 1$, the above expression approximates to

$$Q_{\rm hhh}(\boldsymbol{k}_1,\boldsymbol{k}_2,\boldsymbol{k}_3|M) \approx \frac{Q_{\rm mmm}(\boldsymbol{k}_1,\boldsymbol{k}_2,\boldsymbol{k}_3)}{b_1(M)} + \frac{b_2(M)}{b_1^2(M)}. \quad (30)$$

We now see the utility of the reduced bispectrum: if one constructs halo/galaxy density fields from a local transformation of the matter density, then the lowest order non-linear corrections will lead to a function that is a scaled version of the matter $Q_{\rm mmm}$, plus a constant offset. Moreover, if the density field were simply Gaussian, then estimates of $Q_{\rm hhh}$ on large scales would directly measure b_2/b_1^2.

3 *N*-BODY SIMULATIONS

For our investigations of the bias, we use an ensemble of 40 large N-body simulations, executed on the zBOX-2 and zBOX-3 supercomputers at the University of Zürich. We use only the $z = 0$ outputs from the simulations. Each simulation was performed using the publicly available GADGET-2 code (Springel 2005), and followed the non-linear evolution under gravity of $N = 750^3$ equal-mass particles in a comoving cube of length $L_{\rm sim} = 1500\,h^{-1}$ Mpc.

The cosmological model that we simulated was analogous to the basic vanilla Λ cold dark matter (ΛCDM) model determined by the *WMAP* experiment (Komatsu et al. 2009): matter density $\Omega_{\rm m} = 0.25$, vacuum density $\Omega_\Lambda = 0.75$, power spectrum normalization $\sigma_8 = 0.8$, power spectral index $n = 1$, and dimensionless Hubble parameter $h = 0.7$. The transfer function for the simulations was generated using the publicly available CMBFAST code (Seljak & Zaldarriaga 1996; Seljak et al. 2003), with high sampling of the spatial frequencies on large scales. Initial conditions were set at redshift $z = 49$ using the serial version of the publicly available 2LPT code (Scoccimarro 1998; Crocce, Pueblas & Scoccimarro 2006).

Dark matter halo catalogues were generated for each simulation using the Friends-of-Friends algorithm (Davis et al. 1985), with the linking-length parameter $b = 0.2$, where b is the fraction of the interparticle spacing. For this we employed the fast parallel B-FoF code, provided to us by V. Springel. The minimum number of particles for which an object is considered to be a bound halo was set at 20 particles. This gave a minimum host halo mass of $M_{\rm min} = 1.11 \times 10^{13}\,h^{-1}\,{\rm M}_\odot$. For our analysis of the bias, we use the full sample of haloes and this corresponded to roughly $N^{\rm h} \approx 1.26 \times 10^6$ haloes per simulation. Further details of the simulations may be found in Smith (2009).

4 SIMPLE ESTIMATES OF BIAS

Before we examine halo bias in the context of the bispectrum, we explore two alternative methods for studying the bias. We first evaluate the second-order local biasing model directly, by comparing in a point-wise fashion the halo and matter density fields, smoothed over a range of scales. Then, we use power spectra to determine an effective large-scale bias.

4.1 Analysing density fields

One obvious way to examine the local model of biasing is to simply construct a scatter plot of the local density of dark matter haloes against the local density of dark matter in the simulations (see e.g. Dekel & Lahav 1999; Sheth & Lemson 1999). As was discussed in Section 2.3, this model only makes sense in the context of smooth fields. We shall therefore also inspect how the model parameters depend on the adopted smoothing scale R.

We generate the smoothed density fields as follows: we assign particles/haloes to a Fourier grid using the CIC algorithm (cf. Section 5.1); then we Fourier transform the grid using the fast Fourier transform (FFT) algorithm; each Fourier mode is then multiplied by a Gaussian filter of the form

$$W(kR) \equiv \exp\left[-(kR)^2/2\right]. \quad (31)$$

Finally, on taking the inverse Fourier transform, we obtain the smoothed $\delta(\boldsymbol{x}|R)$ and $\delta^{\rm h}(\boldsymbol{x}|R)$. We perform the above procedure for 28 of the ensemble of simulations and consider the filter scales $R = \{50\,,20\,,10\}\,h^{-1}$ Mpc.

In Fig. 1, we present the bin-averaged scatter plots of $\delta^{\rm h}(\boldsymbol{x}|R)$ versus $\delta(\boldsymbol{x}|R)$, averaged over the realizations. The colour contours are shaded by the normalized population density of that pixel, for example, the central red region indicates that most of the points in the simulation are regions of density close to average. We also see that as the smoothing scale is decreased (panels going from the left-hand to right-hand side) the scatter increases and that there are more points that have higher and lower density. Conversely, as the filter scale is increased, the relation becomes tighter and more linear. One obvious conclusion that may be drawn from this behaviour is that the bias relation is certainly not deterministic.

In order to obtain a more quantitative understanding, we next consider fitting for the parameters of the local bias model at second order. From equation (14) we have

$$\delta_{\rm h}(\boldsymbol{x}|M,R) = b_0(M) + b_1(M)\,\delta(\boldsymbol{x}|R) + \frac{b_2(M)}{2}\left[\delta(\boldsymbol{x}|R)\right]^2. \quad (32)$$

We perform a least-squares analysis on each realization, and then average over the resulting set of bias parameters to obtain the mean parameters: $b_0(M)$, $b_1(M)$ and $b_2(M)$. The 1σ errors are then estimated in the usual way, as quadratic deviations from the sample mean. In Fig. 1, we plot the resultant best-fitting local model as the dot–dashed line in each of the three panels.

The information on the parameters is summarized in Table 1 as a function of the filter scale R. This clearly shows that the estimates of b_1 increase as the smoothing scale is decreased, whereas those for b_2 appear to be parabolical. Naively, one might expect that the non-linear bias terms should approach zero as the amount of smoothing is increased and non-linearities are washed out; however, at $R = 50\,h^{-1}$ Mpc even with $\sigma(x|R) < 1$, the fluctuations are still significant enough to yield a non-zero b_2. Note also that in all cases $b_0 \neq 0$.

The local model, as written in equation (14), asserts that the parameters b_i are independent of the smoothing scale R, and we

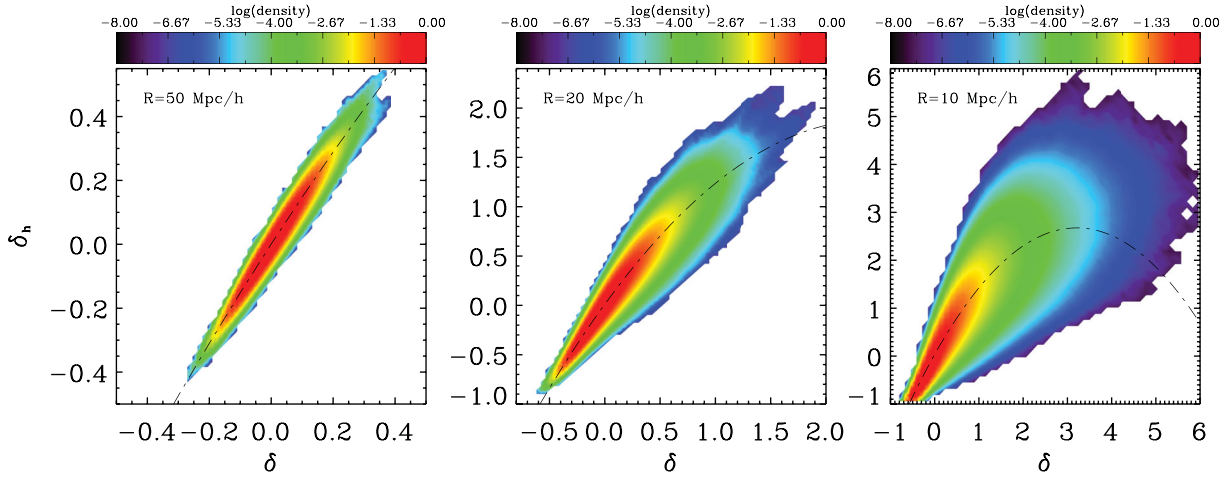

Figure 1. Scatter plots of $\delta_{\rm h}(\boldsymbol{x})$ versus $\delta(\boldsymbol{x})$ smoothed with a Gaussian filter of various scales averaged over the realizations. From the left-hand to right-hand side, the panels correspond to the smoothing scales $R = \{50, 20, 10\}\, h^{-1}$ Mpc, respectively. The colour coding denotes the log of the population density, that is, the red region corresponds to the largest concentration of points and the white background to null values. The dot–dashed line in each panel denotes the local halo bias model up to second order with the best-fitting bias parameters averaged over 28 realizations.

Table 1. Average of the mean bias parameters and the rms errors for the local halo bias model up to second order averaged over 28 realizations determined from fitting the scatter plots of the halo and matter density fields smoothed on scales $k_{\rm s} = \{0.02, 0.05, 0.1\}\, h\,{\rm Mpc}^{-1}$.

R (h^{-1} Mpc)	$b_0 \pm \sigma_{b_0}$ ($\times 10^{-3}$)	$b_1 \pm \sigma_{b_1}$	$b_2 \pm \sigma_{b_2}$
50	1.3 ± 0.1	1.497 ± 0.002	-0.577 ± 0.031
20	12.0 ± 0.1	1.542 ± 0.006	-0.635 ± 0.004
10	37.2 ± 0.1	1.644 ± 0.005	-0.512 ± 0.001

therefore consider the implications as follows. Suppose that non-linear bias is exactly as described by equation (32), but that the coefficients are not independent of the smoothing scale. Let us now consider the results that would be obtained from measurements for two smoothing scales R_a and R_b. From equation (32) we would have

$$\delta_{\rm h}(\boldsymbol{x}|R_a) = b_0^a + b_1^a\,\delta(\boldsymbol{x}|R_a) + \frac{b_2^a}{2}\,[\delta(\boldsymbol{x}|R_a)]^2\,, \tag{33}$$

$$\delta_{\rm h}(\boldsymbol{x}|R_b) = b_0^b + b_1^b\,\delta(\boldsymbol{x}|R_b) + \frac{b_2^b}{2}\,[\delta(\boldsymbol{x}|R_b)]^2. \tag{34}$$

Supposing now that we de-smoothed each of the fields, by Fourier transforming and dividing out the appropriate window function. We would then have

$$\delta_{\rm h}(\boldsymbol{k}) = b_1^a\,\delta(\boldsymbol{k}) + \frac{b_2^a}{2}\int\frac{{\rm d}^3\boldsymbol{q}}{(2\pi)^3}\delta(\boldsymbol{q})\delta(|\boldsymbol{k}-\boldsymbol{q}|)\widetilde{W}_{\boldsymbol{q},\boldsymbol{k}-\boldsymbol{q}}(R_a)\,,$$

$$\delta_{\rm h}(\boldsymbol{k}) = b_1^b\,\delta(\boldsymbol{k}) + \frac{b_2^b}{2}\int\frac{{\rm d}^3\boldsymbol{q}}{(2\pi)^3}\delta(\boldsymbol{q})\delta(|\boldsymbol{k}-\boldsymbol{q}|)\widetilde{W}_{\boldsymbol{q},\boldsymbol{k}-\boldsymbol{q}}(R_b).$$

In order for the above equations to be equivalent, we must have

$$b_1^a = b_1^b\,, \tag{35}$$

$$b_2^a = b_2^b\left[\frac{W(qR_b)}{W(qR_a)}\,\frac{W(|\boldsymbol{k}-\boldsymbol{q}|R_a)}{W(|\boldsymbol{k}-\boldsymbol{q}|R_b)}\,\frac{W(kR_a)}{W(kR_b)}\right]. \tag{36}$$

The last of the above two equations may only be satisfied if and only if $R_a = R_b$ or $\{kR, qR, |\boldsymbol{k}-\boldsymbol{q}|R\} \ll 1$. Since the $\delta^{\rm h}(\boldsymbol{x}|R)$ versus $\delta(\boldsymbol{x}|R)$ method is inherently a real-space measure, it involves contributions from all Fourier modes. It is therefore difficult to ensure that $b_2^a = b_2^b$.

We conclude that the above method will not be a safe way to recover bias parameters independent of the smoothing scale. We now turn to Fourier-space methods.

4.2 Effective large-scale bias from power spectra

We now use various halo power spectra to derive estimates for an *effective* large-scale halo bias.

In order to do this, we first measure the Fourier transform of the matter and halo density fields as described in Appendix A. The halo–halo, halo–mass and mass–mass power spectra, $\{P_{\rm hh}, P_{\rm hm}$ and $P_{\rm mm}\}$, are then estimated from the data by performing the following sums:

$$\widehat{P}_{\mu\nu}(k_l) = \frac{V_\mu}{N(k)}\sum_{m=1}^{N(k)}\delta_\mu(\boldsymbol{k}_l)\delta_\nu^*(\boldsymbol{k}_l), \tag{37}$$

where $\{\mu, \nu\} \in \{{\rm m}, {\rm h}\}$, V_μ is the sample volume (which in our case is the simulation volume), and $N(k)$ are the number of Fourier modes in a shell of thickness Δk.

Following Smith et al. (2007), we next construct the estimators:

$$\widehat{b}_{\rm hh}^{\rm NL} = \frac{1}{N_{\rm s}}\sum_{i=1}^{N_{\rm s}}\sqrt{\frac{\widehat{P}_{\rm hh}(k_i)}{\widehat{P}_{\rm mm}(k_i)}}\,,\quad \widehat{b}_{\rm hh}^{\rm L} = \frac{1}{N_{\rm s}}\sum_{i=1}^{N_{\rm s}}\sqrt{\frac{\widehat{P}_{\rm hh}(k_i)}{P_{\rm mm}^{\rm L}(k_i)}}\,, \tag{38}$$

$$\widehat{b}_{\rm hm}^{\rm NL} = \frac{1}{N_{\rm s}}\sum_{i=1}^{N_{\rm s}}\frac{\widehat{P}_{\rm hm}(k_i)}{\widehat{P}_{\rm mm}(k_i)}\,,\quad \widehat{b}_{\rm hm}^{\rm L} = \frac{1}{N_{\rm s}}\sum_{i=1}^{N_{\rm s}}\frac{\widehat{P}_{\rm hm}(k_i)}{P_{\rm mm}^{\rm L}(k_i)}, \tag{39}$$

where $N_{\rm s}$ is the number of simulations and $P_{\rm mm}^{\rm L}$ is the linear matter power spectrum. Note that in the case of $b_{\rm hh}$ we also consider shot-noise-corrected versions of these two estimators, that is, we correct $P_{\rm hh}$ using equation (A11). We denote these bias estimates by $b_{\rm hh}^{\rm NL,SC}$ and $b_{\rm hh}^{\rm L,SC}$, respectively. Finally, we determine the 1σ errors by evaluating the variance of each realization against the mean.

The left-hand panel of Fig. 2 shows $b_{\rm hh}^{\rm NL}$ (solid blue data points) and $b_{\rm hh}^{\rm NL,SC}$ (open red points). The bias for the shot-noise-corrected terms remains roughly constant at $\sim$1.49 down to scales

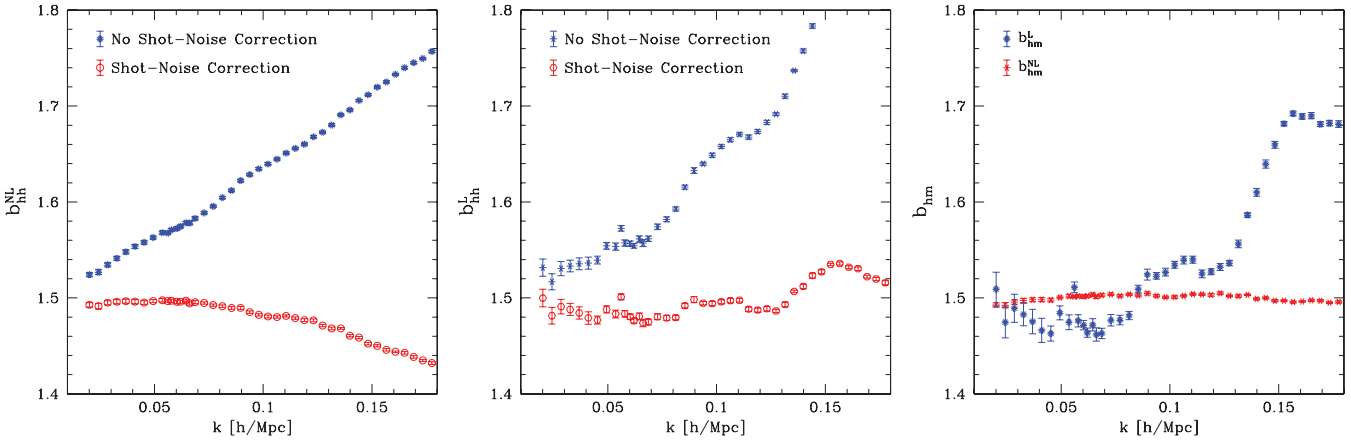

Figure 2. Scale dependence of the effective bias parameters $b_{\rm hh}^{\rm NL}$, $b_{\rm hh}^{\rm L}$, $b_{\rm hm}^{\rm NL}$ and $b_{\rm hm}^{\rm L}$ (cf. equations 38 and 39) estimated from the auto- and cross-power spectra as a function of wavemode. For the left-hand and middle panels: solid blue and open red symbols denote the bias when $P_{\rm hh}$ is not and is shot noise corrected, respectively. The left-hand panel shows $b_{\rm hh}$ when the non-linear matter power spectrum is used; the middle panel shows the same but when the linear matter power spectrum is used; the right-hand panel shows $b_{\rm hm}$, where the red stars and blue points denote the case where the non-linear and linear matter power spectra are used, respectively.

$k \sim 0.08\,h\,{\rm Mpc}^{-1}$ and with very small errors, indicating that the result is highly constrained by the data. On scales smaller than this, the bias is a decreasing function of k. Without shot-noise correction, we find that the bias is strongly scale-dependent, and the bias rapidly increases with increasing k.

The middle panel of Fig. 2 shows the results obtained from using $b_{\rm hh}^{\rm L}$ (solid blue points) and $b_{\rm hh}^{\rm L,SC}$ (open hexagonal points). The results are similar to those for $b_{\rm hh}^{\rm NL,SC}$, but with increased cosmic variance on large scales. An oscillation structure is also present; this can be understood as explained in Guzik, Bernstein & Smith (2007). Nevertheless, comparing the two provides a clear indication of the validity of the tree-level power spectrum up to $k = 0.08\ h\,{\rm Mpc}^{-1}$.

The right-hand panel of Fig. 2 shows the bias results $b_{\rm hm}^{\rm NL}$ (solid red points) and $b_{\rm hm}^{\rm L}$ (solid blue points). The value of $b_{\rm hm}^{\rm NL}$ stays roughly constant for the whole scale range considered in the estimate, while $b_{\rm hm}^{\rm L}$ is not smooth and clearly shows the imprint of the oscillation structure. Nevertheless, we find $b_{\rm hm}^{\rm L} \sim 1.48$, to within the errors for $k < 0.08\,h\,{\rm Mpc}^{-1}$. On comparing the results for $b_{\rm hh}^{\rm NL,SC}$ and $b_{\rm hm}^{\rm NL}$, we see that for scales $k \lesssim 0.08\,h\,{\rm Mpc}^{-1}$ these estimates are compatible and that the effective large-scale bias is roughly $b \sim 1.49$. Interestingly, these findings are consistent with real-space measures of the effective large-scale bias from cell variances (Smith & Marian 2011).

In Table 2, we report the weighted average and corresponding 1σ error on the effective bias, $b_{\rm hh}$, computed over the same k modes corresponding to the magnitude of the third wavevector k_3 for each triangle configuration. The tabulated results for the analysis of the uncorrected data confirm the results shown in Fig. 2 that bias is indeed scale-dependent. Applying the shot-noise correction yields a more constant effective bias, even for the range of k modes entering into our bispectrum estimation. Interestingly, the value $b_1 = 1.49 \pm 0.002$ found for $k \in [0.03, 0.09]$ is in good agreement with the result for b_1 obtained from fitting the density fields smoothed on scales $R = 50\,h^{-1}\,{\rm Mpc}$. Therefore, if we opt to infer that the effective bias is equivalent to b_1 over these scales, then the bispectrum (reduced bispectrum) should also yield this value for b_1 when fitted over the same scale ranges (cf. Table 2), that is, if the local bias model is correct and the tree-level bispectrum (reduced bispectrum) is a sufficient description of the non-linearities on these scales.

Table 2. Weighted average estimates of the effective bias, $b_{\rm hh}$ (see equation 38).

$k\,(h\,{\rm Mpc}^{-1})$	$b_{\rm hh}^{\rm NL}$	$b_{\rm hh}^{\rm NL,SC}$	$b_{\rm hh}^{\rm L}$	$b_{\rm hh}^{\rm L,SC}$
0.03–0.09	1.589 ± 0.002	1.493 ± 0.002	1.589 ± 0.004	1.487 ± 0.004
0.04–0.12	1.624 ± 0.002	1.486 ± 0.002	1.638 ± 0.003	1.489 ± 0.003
0.05–0.15	1.663 ± 0.002	1.474 ± 0.002	1.709 ± 0.003	1.503 ± 0.003
0.06–0.18	1.695 ± 0.001	1.460 ± 0.002	1.775 ± 0.002	1.511 ± 0.003

Before moving on, we point out that one can also use the halo power spectra to define an effective b_2 (Smith, Hernández-Monteagudo & Seljak 2009); however, we shall not explore this here.

5 HALO BIAS FROM BISPECTRA

In this section, we present our main results from the analysis of the halo bispectra.

5.1 Bispectrum estimation

The computational code used to estimate the matter and halo power and bispectra is a modified version of the code developed in Smith et al. (2008), which itself is based on the algorithm of Scoccimarro et al. (1998). The major modification to that code, which we have implemented, is that no random subsampling of the Fourier modes is performed to estimate the bispectrum. Instead, all modes that contribute to a particular triangle configuration are used. In this work, we use a FFT grid of size $N_{\rm g} = 512^3$ to estimate the power and bispectra. We only evaluate triangles that have $k_2 = 2k_1$, but consider the variation of B with the angular separation of the two vectors. The largest scale at which we estimate the bispectrum is $k_1 = 0.03\,h\,{\rm Mpc}^{-1}$, and this is $\approx 7.5 k_{\rm f}$, where $k_{\rm f} = 2\pi/L \approx 0.004\,h\,{\rm Mpc}^{-1}$. Further details of the bispectrum estimation procedure may be found in Appendix A.

Fig. 3 shows the ensemble-averaged shot-noise-corrected results for the halo bispectra $B_{\rm hhh}$ (open red squares) and matter bispectra

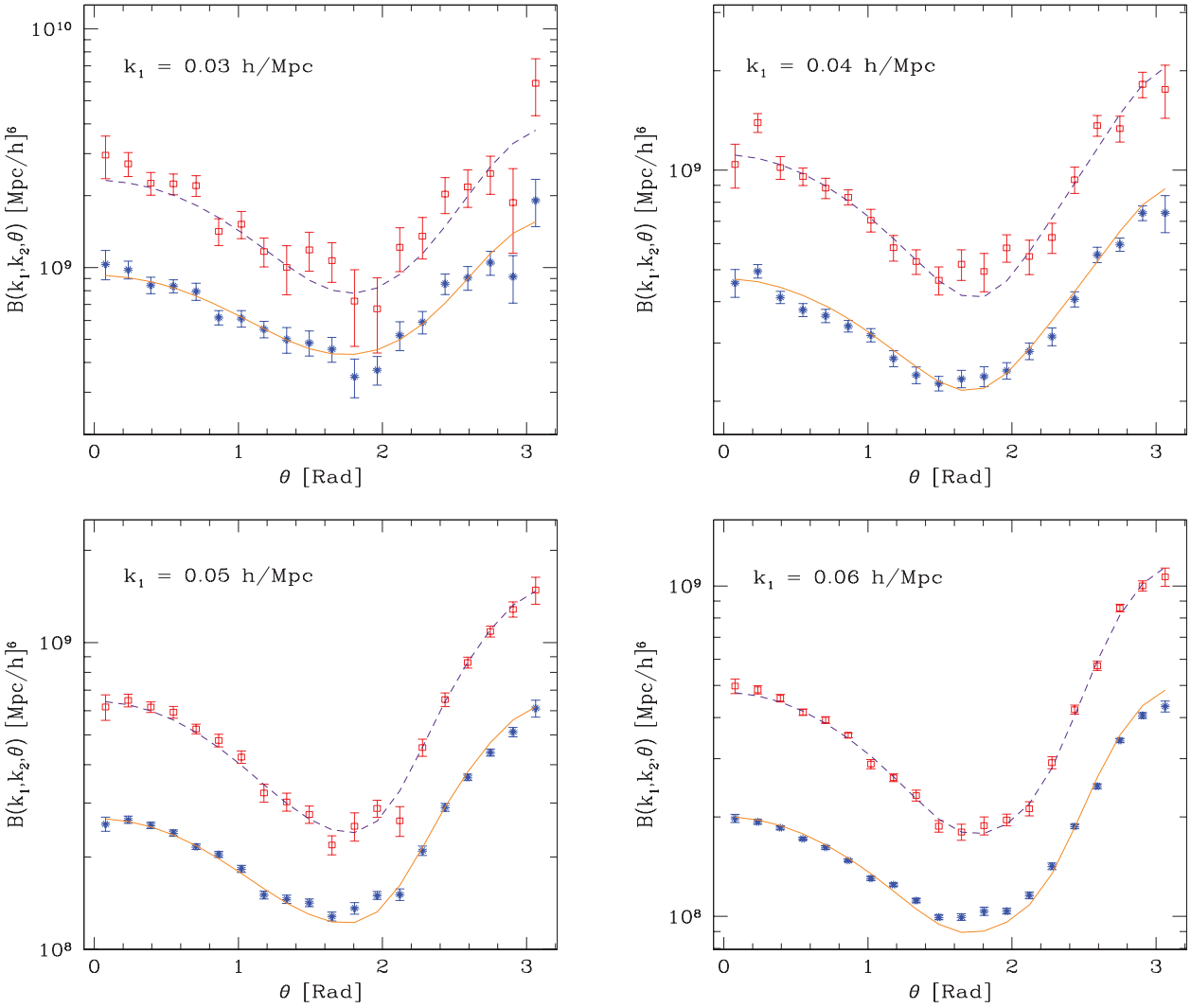

Figure 3. Ensemble-averaged matter and halo bispectrum measurements for 40 ΛCDM N-body simulations in real space in comparison with the PT models at tree level. Each panel shows the shot-noise-corrected bispectrum measurements as a function of angle for a variety of triangle configurations at different scale ranges set by $k_1 = \{0.03\ 0.04\ 0.05\ 0.06\}\,h\,\mathrm{Mpc}^{-1}$ and $k_2 = 2k_1$. The blue solid symbols represent the matter bispectrum, whereas the open squares denote the halo bispectrum. The tree-level bispectrum is represented by the solid orange line, and the local halo bias model with the best-fitting parameters listed in Table 4 is represented by the dashed violet line.

$B_{\rm mmm}$ (solid blue diamonds), measured from the ensemble of N-body simulations. The four panels show the results obtained for the scales: $k_1 = \{0.03, 0.04, 0.05, 0.06\}\,h\,\mathrm{Mpc}^{-1}$. The error bars are the 1σ errors on the mean, derived from the ensemble-to-ensemble variation. The solid red line represents the tree-level prediction for $B_{\rm mmm}$ as given by equation (12). We see that this appears to be a good description of the $B_{\rm mmm}$ estimates for the scales that we have considered. We note that, for the case $k_1 = 0.06\,h\,\mathrm{Mpc}^{-1}$, the theory systematically underpredicts the measurements for $\theta/\pi \sim 0.5$ (but see Section 5.4 for a more quantitative discussion of the goodness-of-fit).

Fig. 4 shows the same as in Fig. 3, however, this time for $Q_{\rm hhh}$ and $Q_{\rm mmm}$.

5.2 Bias estimation

Our method for estimating the bias parameters follows an approach similar to that presented by Scoccimarro (2000) and Porciani & Giavalisco (2002). To start, we take a χ^2 function that is a quadratic form of the type

$$\chi^2(b_1, b_2) = \sum_{i=1}^{N_\theta} \sum_{j=1}^{N_\theta} \Delta_i(b_1, b_2) \widehat{r^{-1}}_{ij} \Delta_j(b_1, b_2), \tag{40}$$

where N_θ is the number of angular bins considered and

$$\Delta_i \equiv \frac{\widehat{\overline{B}}_{\rm hhh}(k_1, k_2, \theta_i) - B^{\rm mod}_{\rm hhh}(k_1, k_2, \theta_i | b_1, b_2)}{\sigma_{\rm hhh}(k_1, k_2, \theta_i)}. \tag{41}$$

Note that in dividing the difference between the estimate of the ensemble average bispectrum ($\widehat{\overline{B}}$) and the model prediction ($B^{\rm mod}$) by the standard deviation ($\sigma_{\rm hhh}$), $\widehat{r^{-1}}_{ij}$ is in fact the inverse correlation matrix. Recall that the correlation and covariance matrices are related by $r_{ij} = C_{ij}/\sqrt{C_{ii}C_{jj}}$.

In order to minimize this χ^2 function and so recover the best-fitting bias parameters, we need an estimate of $\widehat{r^{-1}}_{ij}$, and we do this

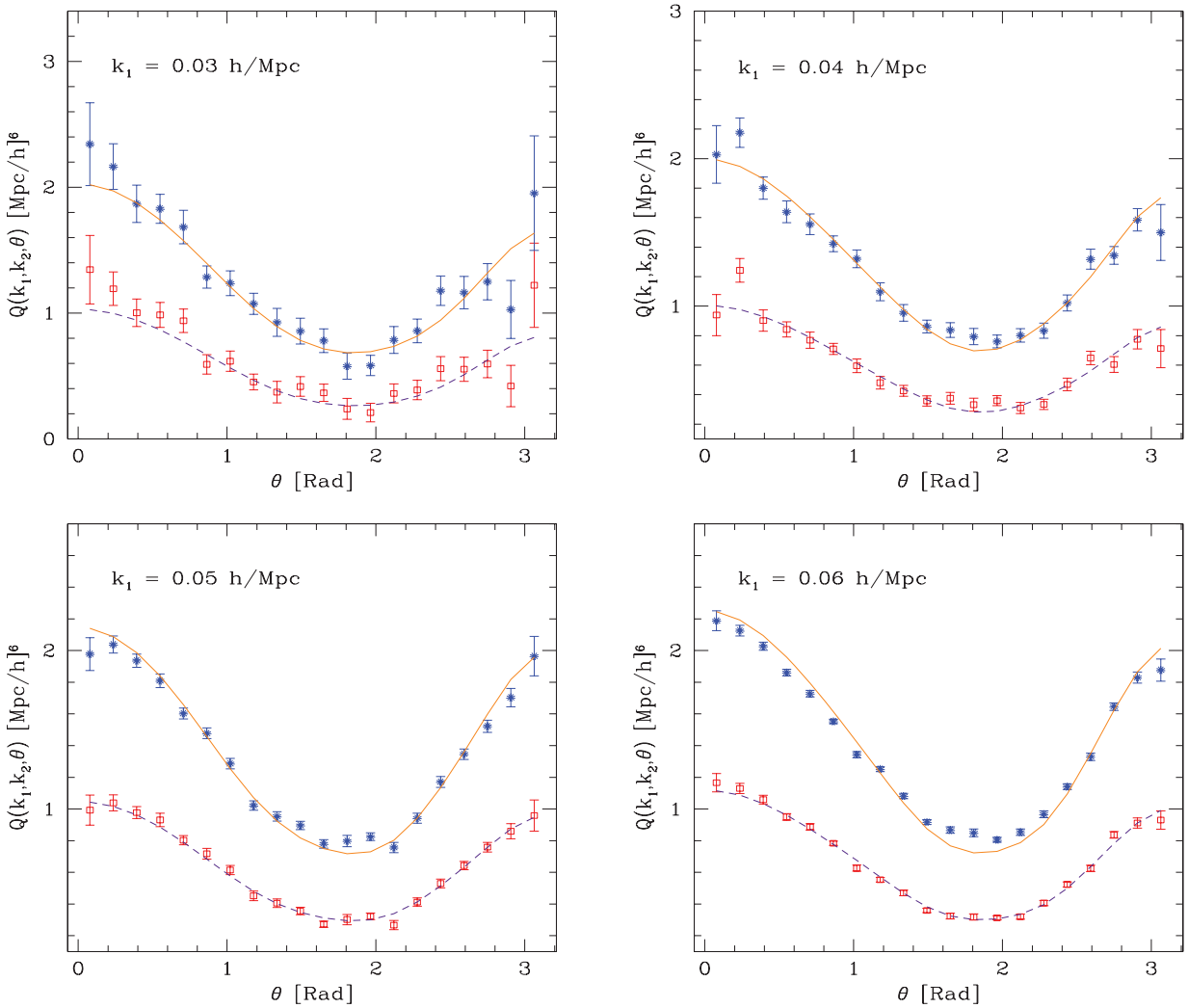

Figure 4. Ensemble-averaged matter and halo-reduced bispectrum measurements of the 40 ΛCDM *N*-body simulations in real space in comparison with the PT models at tree level. The point and line styles are the same as in Fig. 3.

using the standard unbiased estimator

$$\widehat{r}_{ij} = \frac{1}{(N_{\rm sim}-1)} \sum_{k=1}^{N_{\rm sim}} \widetilde{\Delta}_i^k \widetilde{\Delta}_j^k, \tag{42}$$

where $N_{\rm sim}$ is the number of simulations and

$$\widetilde{\Delta}_i \equiv \frac{\widehat{B}_{\rm hhh}^{(k)}(k_1,k_2,\theta_i) - \widehat{\overline{B}}_{\rm hhh}(k_1,k_2,\theta_i)}{\sigma_{\rm hhh}(k_1,k_2,\theta_i)}, \tag{43}$$

where $\widehat{B}_{\rm hhh}^{(k)}$ is the kth estimate of the bispectrum and $\widehat{\overline{B}}_{\rm hhh}$ is the mean of the ensemble.

Next, we use singular value decomposition to invert $\widehat{r}_{ij}$. For the estimate of the inverse correlation matrix, we utilize principal component analysis (PCA) to remove some of the noisy eigenvectors. We select the fraction of principal components that account for 95 per cent of the variance. According to this selection criterion, we typically retain 15 out of 20 of the most 'dominant' eigenmodes. Note that as pointed out in Hartlap, Simon & Schneider (2007), $\widehat{C^{-1}} \neq \widehat{C}^{-1}$. However, since we are using PCA, this should be a subdominant correction. Thus, we may approximate equation (40) to

$$\begin{aligned}\chi^2 &= \sum_{i=1}^{N_\theta}\sum_{j=1}^{N_\theta} \Delta_i(b_1,b_2)[R^{\rm T}\Lambda R]^{-1}_{ij}\Delta_j(b_1,b_2),\\ &= \sum_{i=1}^{N_\theta}\sum_{j=1}^{N_\theta} \Delta_i(b_1,b_2)\sum_{l=1}^{N_\theta} R^{\rm T}_{il}\Lambda^{-1}_{ll}R_{lj}\Delta_j(b_1,b_2),\\ &\approx \sum_{l=1}^{N_\theta} \Lambda^{-1}_{ll}Y_l^2\Theta_{ll},\end{aligned} \tag{44}$$

where the correlation matrix r was diagonalized by rotation into its eigenbasis, that is, $r = R^{\rm T}\Lambda R$, with Λ representing a diagonal matrix of eigenvalues. We also defined $Y_l \equiv \sum_{i=1}^{N_\theta} R_{li}\Delta_i(b_1,b_2)$. Note that in the final approximate expression we include a matrix Θ_{ll}, a diagonal matrix with entries either 1 or 0, depending on whether the eigenvector is to be retained or cut from the PCA reconstruction.

Finally, the $\chi^2(b_1, b_2)$ function was minimized using the Levenberg–Marquardt routine for non-linear least-squares fitting.

5.3 Errors in parameter estimates

To the best-fitting parameters (b_1, b_2), we assign both systematic and statistical errors.

In our context, the systematic errors correspond to the errors induced in the best-fitting parameters from fitting the data with a noisy inverse covariance matrix (or correlation matrix). Owing to the relatively low number of simulations ($N_{\rm sim} = 40$), we expect that equation (42) provides a noisy estimate of r_{ij}^{-1}. In order to estimate the errors this has on the best-fitting parameters, we employ the jackknife subsampling method (see e.g. Norberg et al. 2009). This involves slicing the total data set into $N_{\rm sub}$ subsamples. Then a resampling of the data is obtained by excluding one of the subsamples from the set. From this resampling, we then estimate the mean statistic of interest and the inverse correlation matrix as described in the previous section. The resampled data set is then used to determine a new estimate of the best-fitting bias parameters. This procedure is then repeated for all of the possible $N_{\rm sub}$ resamplings of the data. In our particular case, we treat the measurements from each simulation as the regions to be included or excluded, and this gives us 40 jackknife estimates of the bias parameters (b_1, b_2). The parameter covariance matrix for the systematic errors can be computed as (Norberg et al. 2009)

$$\widehat{C}^{\rm JK}[b_i, b_j] = \frac{N_{\rm sub}-1}{N_{\rm sub}} \sum_{k=1}^{N_{\rm sub}} (b_{i,k} - \hat{\bar{b}}_j)(b_{j,k} - \hat{\bar{b}}_j), \tag{45}$$

where $b_{i,k}$ is the estimate of b_i from the kth resampling of the data and $\hat{\bar{b}}_i$ is the estimate of the mean b_i obtained from all of the resamplings.

The statistical error is obtained directly from the non-linear least-squares analysis. The routine `mrqmin` provides an approximation to the errors on the parameters that corresponds to a $\Delta\chi^2 \approx 1$ for a one-parameter model. However, the confidence regions we present in the forthcoming plots correspond to either $\Delta\chi^2 = (2.30, 6.17)$, which roughly denote the ($\sim 1\sigma$, $\sim 2\sigma$) errors for a two-parameter model.

Given that we consider two forms of error, systematic and statistical, and that one is never consistently larger than the other, in all forthcoming tables, we choose to report only the total error. This is obtained simply from the two errors added in quadrature.

5.4 Testing the validity of the tree-level matter *B*

Before we report the estimates of the halo bias parameters, we first present a test of the validity of the tree-level model for the matter bispectrum. We do this by applying the χ^2 test described above, to the $B_{\rm mmm}$ and $Q_{\rm mmm}$ data, and so fit for b_1 and b_2. Note that since the total number of principal components retained equals 15, for a two-parameter model, the number of degrees of freedom equals 13. If the tree-level expressions in the large-scale limit as given by equations (26) and (30) are correct, then we should expect to find $b_1 = 1$ and $b_2 = 0$.

Table 3 presents the best-fitting non-linear bias parameters for the four different bispectrum scale ranges discussed earlier. In the analysis, we fit the shot-noise-corrected bispectra. The χ^2 values (last column of the table) confirm that the tree-level expressions $B^0_{\rm mmm}$ and $Q^0_{\rm mmm}$ provide good fits for the triangle configurations with $k_1 = \{0.03, 0.04\}\,h\,{\rm Mpc}^{-1}$. However, for $k_1 = \{0.05, 0.06\}\,h\,{\rm Mpc}^{-1}$, the fits are poor, given the χ^2 estimates, and we see that, for both B and Q, they yield non-zero values for b_2 at 1σ. The results also imply that the failure of the tree-level model on these scales is more severe for Q than for B. This can be understood by noting that b_1 from $Q_{\rm mmm}$ shows a prominent departure from unity, whereas $B_{\rm mmm}$ does not (although the deviation still exceeds 2σ). We thus conclude that it is likely that the tree-level expressions for the halo bispectra will only be valid for $k_1 \leq 0.04\,h\,{\rm Mpc}^{-1}$, for our chosen bispectrum configurations.

Table 3. Assessment of the validity of the tree-level modelling by fitting the matter bispectra and reduced bispectra. Column (1): bispectrum triangle scale; column (2): statistic, where $B_{\rm mmm}$ and $Q_{\rm mmm}$ are shot-noise corrected; columns (3) and (4): best-fitting b_1 and b_2 along with 1σ errors; column (5): χ^2.

k_1 ($h\,{\rm Mpc}^{-1}$)		$b_1 \pm \sigma_{b_1}$	$b_2 \pm \sigma_{b_2}$	χ^2
0.03	$B_{\rm mmm}$	1.01 ± 0.07	-0.04 ± 0.25	19.08
	$Q_{\rm mmm}$	0.93 ± 0.19	-0.05 ± 0.30	19.03
0.04	$B_{\rm mmm}$	0.98 ± 0.03	0.04 ± 0.10	14.31
	$Q_{\rm mmm}$	1.05 ± 0.09	0.07 ± 0.16	14.95
0.05	$B_{\rm mmm}$	0.97 ± 0.02	0.13 ± 0.08	38.83
	$Q_{\rm mmm}$	1.14 ± 0.07	0.19 ± 0.13	19.97
0.06	$B_{\rm mmm}$	0.98 ± 0.02	0.10 ± 0.10	34.09
	$Q_{\rm mmm}$	1.15 ± 0.04	0.22 ± 0.08	29.58

5.5 Constraints on b_1 and b_2 from halo bispectra

Table 4 presents the best-fitting non-linear bias parameters and their respective 1σ errors in quadrature, obtained from the χ^2 analysis of $B_{\rm hhh}$ and $Q_{\rm hhh}$. Note that we present the results for both the uncorrected and shot-noise-corrected measurements, indicated in the table by superscript 'SC'. Table 4 also shows the χ^2 value of these best-fitting parameters as an indication of the goodness-of-fit.

In Figs 3 and 4, we also show the tree-level theoretical models for $B_{\rm hhh}$ and $Q_{\rm hhh}$ (dashed lines), where the best-fitting bias parameters from Table 4 have been used. These figures demonstrate that, at least by eye, the tree-level models provide a reasonable description of the data. However, a more detailed inspection of Table 4 reveals some important discrepancies.

Table 4. Best-fitting bias parameters from fitting the halo–halo–halo bispectra and reduced bispectra. Column (1): bispectrum triangle scale; column (2): statistic, where $B_{\rm hhh}$ and $Q_{\rm hhh}$ are raw, and $B^{\rm SC}_{\rm hhh}$ and $Q^{\rm SC}_{\rm hhh}$ are shot noise corrected; columns (3) and (4): best-fitting b_1 and b_2 along with 1σ errors; column (5): χ^2.

k_1 ($h\,{\rm Mpc}^{-1}$)		$b_1 \pm \sigma_{b_1}$	$b_2 \pm \sigma_{b_2}$	χ^2
0.03	$B_{\rm hhh}$	1.43 ± 0.11	-0.18 ± 0.40	17.20
	$B^{\rm SC}_{\rm hhh}$	1.42 ± 0.11	-0.36 ± 0.38	17.08
	$Q_{\rm hhh}$	2.09 ± 0.55	-0.12 ± 0.76	16.08
	$Q^{\rm SC}_{\rm hhh}$	1.75 ± 0.47	-0.39 ± 0.56	16.66
0.04	$B_{\rm hhh}$	1.41 ± 0.08	-0.05 ± 0.26	26.92
	$B^{\rm SC}_{\rm hhh}$	1.38 ± 0.08	-0.27 ± 0.25	26.16
	$Q_{\rm hhh}$	2.32 ± 0.39	0.14 ± 0.58	26.40
	$Q^{\rm SC}_{\rm hhh}$	1.80 ± 0.29	-0.34 ± 0.36	26.96
0.05	$B_{\rm hhh}$	1.40 ± 0.06	0.15 ± 0.21	31.92
	$B^{\rm SC}_{\rm hhh}$	1.38 ± 0.05	-0.25 ± 0.15	12.63
	$Q_{\rm hhh}$	2.66 ± 0.26	0.57 ± 0.42	11.53
	$Q^{\rm SC}_{\rm hhh}$	1.90 ± 0.19	-0.30 ± 0.22	11.60
0.06	$B_{\rm hhh}$	1.41 ± 0.05	0.19 ± 0.24	63.64
	$B^{\rm SC}_{\rm hhh}$	1.37 ± 0.03	-0.23 ± 0.13	19.30
	$Q_{\rm hhh}$	2.84 ± 0.20	0.88 ± 0.40	20.70
	$Q^{\rm SC}_{\rm hhh}$	1.87 ± 0.14	-0.30 ± 0.19	19.47

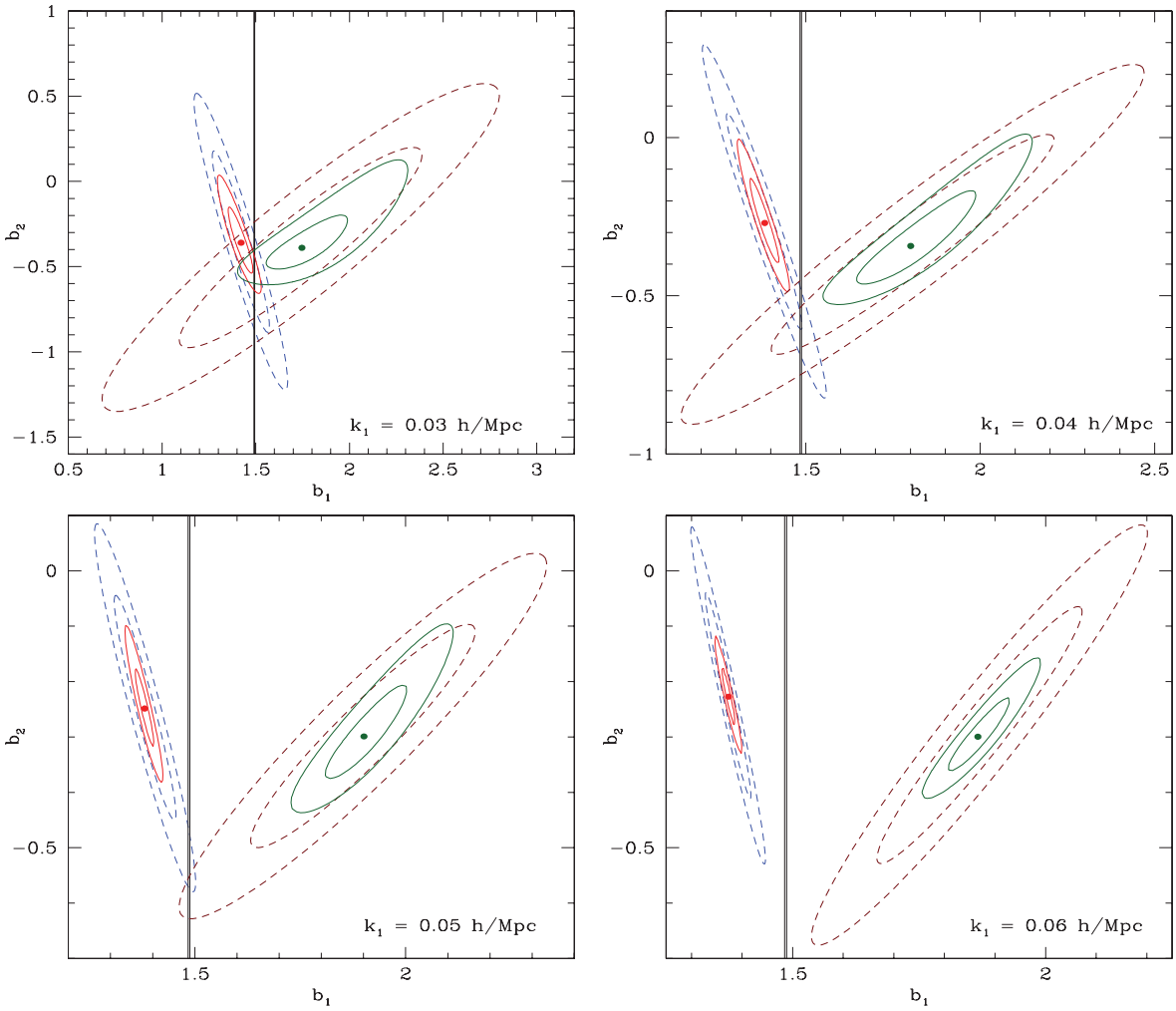

Figure 5. Evolution of the likelihood contours for the bias parameters b_1 and b_2, estimated from $B_{\rm hhh}$ and $Q_{\rm hhh}$, with scale. The solid lines denote the 68 and 95 per cent confidence intervals, obtained from a full exploration of the likelihood surface around the best-fitting values; the dashed lines denote the same, but where the jackknife parameter covariance matrix from equation (45) has been used to determine the error contours. The top left-hand, top right-hand, bottom left-hand and bottom right-hand panels show the results for triangle configurations with $k_1 = \{0.03, 0.04, 0.05, 0.06\}\,h\,{\rm Mpc}^{-1}$, respectively. The vertical black lines denote the effective bias parameter $b_{\rm hh}^{\rm NL,SC}$, using the same wavemodes as that enter into the bispectrum estimates.

For the case of fitting B, the shot-noise correction is less important, as we see that the estimates of b_1 for all bispectrum configurations with and without shot-noise corrections are consistent to within the errors, and have $b_1 \sim 1.4$. However, b_2 shows systematic differences, being more negative if the correction is made, and for this we find that $b_2 \sim -0.25$. On the other hand, for the case of Q, the results clearly show that the shot-noise subtraction has an important effect on the recovered values for the bias parameters. If the shot noise is not corrected, then we see that the estimates for b_1 increase systematically as we go from triangle configurations with $k_1 = 0.03$ to $0.06\,h\,{\rm Mpc}^{-1}$, whereas if it is corrected, then we find $b_1 \sim 1.8$ and $b_2 \sim -0.3$ to within the errors. On comparing the results from B and Q, we see that, whilst the values for b_1 disagree significantly, surprisingly, the values for b_2 remain consistent at the 1σ level.

The χ^2 function of equation (41) may be interpreted as a Gaussian likelihood if we make the transformation, $\mathcal{L}(\{B_{\rm hhh}\}|b_1, b_2) \propto \exp[-\chi^2/2]$. Once suitably normalized and on assuming a set of prior probabilities, we may then explore the shape of the confidence regions in the posterior probability $p(b_1, b_2|\{B_{\rm hhh}\})$.

Fig. 5 shows the 1σ likelihood confidence contours in the posterior probability for the non-linear bias parameters for the four scales considered according to our method of analysis described above. The solid lines denote the size of the confidence regions at the 68 and 95 per cent level (i.e. $\Delta\chi^2 \approx 2.3, 6.17$) when we construct a correlation matrix from the 40 realizations without regard to the systematic uncertainty. The dashed lines demonstrate the magnitude at which the 68 and 95 per cent confidence regions expand following our generation of a set of jackknife subsamples to monitor the effect due to the implicit error associated with the estimated correlation matrix. Hence, we clearly see the relevance of accounting for the uncertainty of the correlation matrix when obtaining the bias parameter constraints. The discrepancy between the resulting jackknife error ellipses for B and Q is less severe than the likelihood contours obtained from the complete sample where the level of agreement improves progressing to large scales, yet this might be due to the fact that the statistical error is more prominent at larger scales. Interestingly, the overlap of the two likelihood regions at 2σ for k_1=0.03, 0.04 and 0.05 $h\,{\rm Mpc}^{-1}$ occurs with the rectangular region or strip denoting the effective bias measure, $b_{\rm hh}^{\rm NL,SC}$, at 1σ. This

set of panels in Fig. 5 convey pictorially the information obtained from the results in Table 4 that the likelihood contours from analysis of Q show an evolution with decreasing scale towards larger and larger b_1, whereas the constraints on b_2 remain consistent. Finally, the constraints obtained from analysing the Q amplitudes are much weaker than those coming from the bispectrum.

6 HALO BIAS FROM CROSS-BISPECTRA

In Section 5.5, we saw that shot-noise corrections influenced the recovery of the bias parameters particularly for Q. In this section, we attempt to develop the use of cross-bispectra, as measures of the bias that are less susceptible to discreteness effects. The use of cross-correlations in large-scale structure work has long been known as a way of reducing discreteness corrections (Peebles 1980). However, it is only relatively recent that it has been applied to study bias (Smith et al. 2007; Dalal et al. 2008; Desjacques, Seljak & Iliev 2009; Padmanabhan et al. 2009; Smith 2009; Pillepich, Porciani & Hahn 2010).

6.1 Definitions and theory

We may define the halo cross-bispectra as follows:

$$\langle\delta_{\rm h}(\boldsymbol{k}_1)\delta_{\rm h}(\boldsymbol{k}_2)\delta(\boldsymbol{k}_3)\rangle = (2\pi)^3\,\delta^{\rm D}(\boldsymbol{k}_{123})B_{\rm hhm}(\boldsymbol{k}_1,\boldsymbol{k}_2,\boldsymbol{k}_3)\,, \tag{46}$$

$$\langle\delta_{\rm h}(\boldsymbol{k}_1)\delta(\boldsymbol{k}_2)\delta(\boldsymbol{k}_3)\rangle = (2\pi)^3\,\delta^{\rm D}(\boldsymbol{k}_{123})B_{\rm hmm}(\boldsymbol{k}_1,\boldsymbol{k}_2,\boldsymbol{k}_3). \tag{47}$$

We then symmetrize these quantities by the operations

$$B^{\rm (sym)}_{\rm hhm} = \left[B_{\rm hhm} + B_{\rm hmh} + B_{\rm mhh}\right]/3\,, \tag{48}$$

$$B^{\rm (sym)}_{\rm hmm} = \left[B_{\rm hmm} + B_{\rm mhm} + B_{\rm mmh}\right]/3. \tag{49}$$

For ease of notation, we shall now simply take $B^{\rm (sym)}_{\rm hhm} \equiv B_{\rm hhm}$ and $B^{\rm (sym)}_{\rm hmm} \equiv B_{\rm hmm}$, unless otherwise indicated. We may now also define the cross-reduced bispectra as

$$Q_{\rm hhm} \equiv B_{\rm hhm}/PP_{\rm hhm}\,, \tag{50}$$

$$Q_{\rm hmm} \equiv B_{\rm hmm}/PP_{\rm hmm}, \tag{51}$$

where we have for the denominators (again symmetrized)

$$PP_{\rm hhm} = \frac{2}{3}\left[P_{\rm hh}(k_1)P_{\rm hm}(k_2) + 2\,{\rm cyc}\right] + \frac{1}{3}\left[P_{\rm hm}(k_1)P_{\rm hm}(k_2) + 2\,{\rm cyc}\right]\,, \tag{52}$$

$$PP_{\rm hmm} = \frac{2}{3}\left[P_{\rm hm}(k_1)P_{\rm mm}(k_2) + 2\,{\rm cyc}\right] + \frac{1}{3}\left[P_{\rm hm}(k_1)P_{\rm hm}(k_2) + 2\,{\rm cyc}\right]. \tag{53}$$

The relations for $PP_{\rm hhm}$ and $PP_{\rm hmm}$ can easily be constructed using a graphical approach. Let us consider three nodes two of which are the same and the third is different (we shall think of the nodes as the density fields). Label these nodes 1, 2 and 3. Now consider all possible ways to connect the three nodes together by two edges. When the two nodes, which are the same, connect together, this gives us an auto-power spectrum with a delta function, and when two nodes that are different connect together, this gives us a cross-power spectrum and delta function. One may then symmetrize the results by considering all possible re-labellings of the nodes and dividing by three.

In Appendix B, we calculate the tree-level cross-bispectra, $B_{\rm hmm}$ and $B_{\rm hhm}$, in the local model of halo biasing. The main results are

$$B^{(0)}_{\rm hmm}(\boldsymbol{k}_1,\boldsymbol{k}_2,\boldsymbol{k}_3) \approx b_1(M)B^{(0)}_{\rm mmm}(\boldsymbol{k}_1,\boldsymbol{k}_2,\boldsymbol{k}_3) + \frac{b_2(M)}{3}\left[\widetilde{W}_{k_1,k_2}P^{(0)}_{\rm mm}(k_1)P^{(0)}_{\rm mm}(k_2) + 2\,{\rm cyc}\right]\,, \tag{54}$$

$$B^{(0)}_{\rm hhm}(\boldsymbol{k}_1,\boldsymbol{k}_2,\boldsymbol{k}_3) \approx b_1^2(M)B^{(0)}_{\rm mmm}(\boldsymbol{k}_1,\boldsymbol{k}_2,\boldsymbol{k}_3) + \frac{1}{3}b_1(M) \times b_2(M)\left[\widetilde{W}_{k_1,k_2}P^{(0)}_{\rm mm}(k_1)P^{(0)}_{\rm mm}(k_2) + 2\,{\rm cyc}\right]. \tag{55}$$

In the limit of large scales, and/or small smoothing scales, the filter functions $\widetilde{W}_{k_1,k_2} \to 1$ and we have

$$B^{(0)}_{\rm hmm} \approx b_1 B^{(0)}_{\rm mmm} + \frac{b_2}{3}\left[P^{(0)}_{\rm mm}(k_1)P^{(0)}_{\rm mm}(k_2) + 2\,{\rm cyc}\right]\,, \tag{56}$$

$$B^{(0)}_{\rm hhm} \approx b_1^2 B^{(0)}_{\rm mmm} + \frac{1}{3}b_1 b_2\left[P^{(0)}_{\rm mm}(k_1)P^{(0)}_{\rm mm}(k_2) + 2\,{\rm cyc}\right]. \tag{57}$$

At second order in the non-linear bias and PT, the cross-reduced bispectra are

$$Q^{(0)}_{\rm hmm} \approx \frac{3Q_{\rm mmm}}{2 + b_1(M)} + \frac{b_2(M)}{2b_1(M) + b_1^2(M)}\alpha(\boldsymbol{k}_1,\boldsymbol{k}_2,\boldsymbol{k}_3)\,, \tag{58}$$

$$Q^{(0)}_{\rm hhm} \approx \frac{3\,Q_{\rm mmm}}{2b_1(M) + 1} + \frac{2b_2(M)}{2b_1^2(M) + b_1(M)}\alpha(\boldsymbol{k}_1,\boldsymbol{k}_2,\boldsymbol{k}_3). \tag{59}$$

In the large-scale limit, $\alpha \to 1$, these expressions become

$$Q^{(0)}_{\rm hmm} \approx \frac{3Q_{\rm mmm}}{2 + b_1(M)} + \frac{b_2(M)}{2b_1(M) + b_1^2(M)}\,, \tag{60}$$

$$Q^{(0)}_{\rm hhm} \approx \frac{3\,Q_{\rm mmm}}{2b_1(M) + 1} + \frac{2b_2(M)}{2b_1^2(M) + b_1(M)}. \tag{61}$$

6.2 Estimation of the cross-bispectra

The cross-bispectra $B_{\rm hhm}$ and $B_{\rm hmm}$ can be estimated following the algorithm described in Section 5.1 with some small modifications. First, the estimates must be symmetrized, and for the discrete form of $B_{\rm hhm}$ we have

$$\widehat{B}^{\rm d}_{\rm hhm}(k_1,k_2,\theta_{12}) = \frac{1}{3}\frac{V_\mu^2}{N_{\rm tri}}\sum_{(\boldsymbol{n}_1,\boldsymbol{n}_2)}^{N_{\rm tri}} \times\left\{\mathcal{R}e[\delta_{\rm h}(\boldsymbol{k}_{\boldsymbol{n}_1})\delta_{\rm h}(\boldsymbol{k}_{\boldsymbol{n}_2})\delta_{\rm m}(\boldsymbol{k}_{\boldsymbol{n}_3})] + 2\,{\rm cyc}\right\}, \tag{62}$$

and similarly for $\widehat{B}^{\rm d}_{\rm hmm}$. The reduced bispectra are estimated by dividing the above bispectrum estimates by estimates for $PP_{\rm hhm}$ and $PP_{\rm hmm}$ from equations (52) and (53), respectively.

One further complication is constructing the corrections for shot noise. This may be performed following the Counts-in-Cells approach of Peebles (1980) (see also Smith 2009). We find that the symmetrized corrections for $B_{\rm hhm}$ and $B_{\rm hmm}$ can be written as

$$\widehat{\widehat{B}}_{\rm hhm,shot} \equiv \frac{1}{3\overline{n}_{\rm h}}\left[P^{\rm d}_{\rm hm}(k_1) + 2\,{\rm cyc}\right]\,, \tag{63}$$

$$\widehat{\widehat{B}}_{\rm hmm,shot} \equiv \frac{1}{3\overline{n}_{\rm m}}\left[P^{\rm d}_{\rm hm}(k_1) + 2\,{\rm cyc}\right], \tag{64}$$

where $\overline{n}_{\rm m} = N/V_\mu$ and $\overline{n}_{\rm h} = N_{\rm h}/V_\mu$ are the number density of matter particles and haloes, respectively. For the reduced bispectra,

we must correct the estimates of $PP_{\rm hhm}$ and $PP_{\rm hmm}$, which are written in the following form:

$$Q^{\rm denom}_{\rm hhm,shot} = \frac{2}{3\overline{n}_{\rm h}}\left[\widehat{P}^{\rm d}_{\rm hm}(k_1) + 2\,{\rm cyc}\right], \quad (65)$$

$$Q^{\rm denom}_{\rm hmm,shot} = \frac{2}{3\overline{n}_{\rm m}}\left[\widehat{P}^{\rm d}_{\rm hm}(k_1) + 2\,{\rm cyc}\right]. \quad (66)$$

As it is the case that $\overline{n}_{\rm m} \gg \overline{n}_{\rm h}$, we expect that the shot-noise corrections to $B_{\rm hmm}$ will be significantly smaller than for $B_{\rm hhm}$. Hence, we shall think of this as being an almost perfect measure independent of discreteness.

Using these estimators, we compute the ensemble average and ensemble-to-ensemble variations of the halo–mass cross-bispectra. We do this for the same bispectrum configurations as were considered in Section 5.1.

6.3 Non-linear bias from cross-bispectra

We estimate the non-linear bias parameters and their errors from the cross-bispectra using the same method as employed for the auto-bispectra in Sections 5.2 and 5.3. The results are tabulated in Tables 5 and 6, respectively.

Fig. 6 presents the 2D 95 per cent confidence likelihood contours for b_1 and b_2 that are obtained from fitting the shot-noise-corrected bispectra $\{B^{\rm SC}_{\rm hhh}, B^{\rm SC}_{\rm hhm}, B^{\rm SC}_{\rm hmm}\}$ and reduced bispectra $\{Q^{\rm SC}_{\rm hhh}, Q^{\rm SC}_{\rm hhm}, Q^{\rm SC}_{\rm hmm}\}$. The four panels show the results obtained from fitting triangle configurations, $k_1 \in \{0.03, 0.04, 0.05, 0.06\}\,h\,{\rm Mpc}^{-1}$, with $k_2/k_1 = 2$, and these correspond to the top left-hand, top right-hand, bottom left-hand and bottom right-hand panels, respectively. For comparative purposes, the vertical band in each panel denotes the 1σ constraint on $b^{\rm NL,SC}_{\rm hh}$, obtained from the shot-noise-corrected halo and non-linear matter power spectra (cf. Section 4.2).

Considering first the bispectra $\{B^{\rm SC}_{\rm hmm}, B^{\rm SC}_{\rm hhm}, B^{\rm SC}_{\rm hhh}\}$ (solid red lines of increasing thickness), from the figure and the tables, we see that all the results are reasonably consistent with one another over the various scale ranges considered. However, when smaller scales are used (i.e. $k_1 \geq 0.05\,h\,{\rm Mpc}^{-1}$), the consistency weakens and the best-fitting parameters, obtained from $B^{\rm SC}_{\rm hhh}$ and $B^{\rm SC}_{\rm hmm}$, differ by $\gtrsim 2.5\sigma$.

Evaluating the results for the reduced bispectra $\{Q^{\rm SC}_{\rm hmm}, Q^{\rm SC}_{\rm hhm}, Q^{\rm SC}_{\rm hhh}\}$ (dashed blue lines of increasing thickness), the four panels show a strong evolution of the error ellipses with scale. We also note that the level of agreement between the different estimators also evolves strongly, becoming weaker and weaker as smaller scales are considered. At the largest scale where $k = 0.03\,h\,{\rm Mpc}^{-1}$, all the 2σ likelihood contour regions overlap. However, this consistency is broken for the next scale range, $k = 0.04\,h\,{\rm Mpc}^{-1}$, where $Q_{\rm hmm}$ and $Q_{\rm hhm}$ are shifted downwards and farther to the right-hand side, favouring a more negative b_2 and higher b_1. The trend continues in this same direction heading to smaller and smaller scales.

Comparing the results from both B and Q together, we see that only on the largest scales is there any degree of overall consistency. One way to interpret the results up to now is that if we believe $b_1 \approx b^{\rm NL,SC}_{\rm hh}$, then the agent driving the inconsistency between the parameter estimates is the breakdown of the local bias model at tree level. Furthermore, the breakdown of the local tree-level model is more severe for the reduced bispectrum than for the bispectrum.

Table 5. Best-fitting bias parameters from halo–mass–mass bispectra and reduced bispectra. Column (1): bispectrum triangle scale; column (2): statistic, where $B_{\rm hmm}$ and $Q_{\rm hmm}$ are raw, and $B^{\rm SC}_{\rm hmm}$ and $Q^{\rm SC}_{\rm hmm}$ are shot noise corrected; columns (3) and (4): best-fitting b_1 and b_2 along with 1σ errors; column (5): χ^2.

$k_1\,(h\,{\rm Mpc}^{-1})$		$b_1 \pm \sigma_{b_1}$	$b_2 \pm \sigma_{b_2}$	χ^2
0.03	$B_{\rm hmm}$	1.37 ± 1.18	-0.36 ± 0.32	16.86
	$B^{\rm SC}_{\rm hmm}$	1.37 ± 1.18	-0.36 ± 0.32	16.86
	$Q_{\rm hmm}$	1.98 ± 0.75	-0.75 ± 0.99	19.09
	$Q^{\rm SC}_{\rm hmm}$	1.98 ± 0.75	-0.75 ± 0.99	19.09
0.04	$B_{\rm hmm}$	1.33 ± 0.16	-0.33 ± 0.51	16.83
	$B^{\rm SC}_{\rm hmm}$	1.33 ± 0.16	-0.33 ± 0.51	16.83
	$Q_{\rm hmm}$	2.50 ± 0.56	-0.31 ± 0.89	17.96
	$Q^{\rm SC}_{\rm hmm}$	2.51 ± 0.56	-0.32 ± 0.89	17.97
0.05	$B_{\rm hmm}$	1.30 ± 0.07	-0.01 ± 0.23	26.98
	$B^{\rm SC}_{\rm hmm}$	1.30 ± 0.07	-0.02 ± 0.23	26.82
	$Q_{\rm hmm}$	2.94 ± 0.25	0.24 ± 0.57	16.90
	$Q^{\rm SC}_{\rm hmm}$	2.94 ± 0.25	0.23 ± 0.57	16.95
0.06	$B_{\rm hmm}$	1.29 ± 0.07	-0.001 ± 0.28	13.99
	$B^{\rm SC}_{\rm hmm}$	1.29 ± 0.07	-0.004 ± 0.28	13.93
	$Q_{\rm hmm}$	3.45 ± 0.30	1.43 ± 0.94	46.60
	$Q^{\rm SC}_{\rm hmm}$	3.45 ± 0.30	1.42 ± 0.94	46.87

Table 6. Best-fitting bias parameters from halo–halo–mass bispectra and reduced bispectra. Column (1): bispectrum triangle scale; column (2): statistic, where $B_{\rm hhm}$ and $Q_{\rm hhm}$ are raw, and $B^{\rm SC}_{\rm hhm}$ and $Q^{\rm SC}_{\rm hhm}$ are shot noise corrected; columns (3) and (4): best-fitting b_1 and b_2 along with 1σ errors; column (5): χ^2.

$k_1\,(h\,{\rm Mpc}^{-1})$		$b_1 \pm \sigma_{b_1}$	$b_2 \pm \sigma_{b_2}$	χ^2
0.03	$B_{\rm hhm}$	1.42 ± 0.25	-0.32 ± 0.60	17.13
	$B^{\rm SC}_{\rm hhm}$	1.42 ± 0.24	-0.45 ± 0.47	17.49
	$Q_{\rm hhm}$	2.08 ± 0.40	-0.49 ± 0.46	17.45
	$Q^{\rm SC}_{\rm hhm}$	2.11 ± 0.40	-0.67 ± 0.42	17.46
0.04	$B_{\rm hhm}$	1.39 ± 0.14	-0.24 ± 0.25	21.29
	$B^{\rm SC}_{\rm hhm}$	1.37 ± 0.15	-0.37 ± 0.24	21.42
	$Q_{\rm hhm}$	2.49 ± 0.46	-0.17 ± 0.56	22.92
	$Q^{\rm SC}_{\rm hhm}$	2.56 ± 0.49	-0.47 ± 0.51	24.60
0.05	$B_{\rm hhm}$	1.38 ± 0.08	-0.05 ± 0.18	22.46
	$B^{\rm SC}_{\rm hhm}$	1.36 ± 0.07	-0.29 ± 0.14	13.16
	$Q_{\rm hhm}$	2.87 ± 0.18	0.22 ± 0.29	12.55
	$Q^{\rm SC}_{\rm hhm}$	2.92 ± 0.19	-0.37 ± 0.25	16.77
0.06	$B_{\rm hhm}$	1.39 ± 0.07	-0.07 ± 0.25	20.56
	$B^{\rm SC}_{\rm hhm}$	1.36 ± 0.07	-0.31 ± 0.22	15.32
	$Q_{\rm hhm}$	3.12 ± 0.27	0.54 ± 0.52	37.81
	$Q^{\rm SC}_{\rm hhm}$	3.25 ± 0.31	-0.14 ± 0.47	60.54

7 THE NEED FOR BEYOND-TREE-LEVEL BIAS MODELS

This final set of analysis consists of a simple proof of method test, and we determine whether, when the underlying bias model is known, the 'true' bias parameters of the model are indeed recoverable with our approach.

7.1 Biasing by hand

For these tests, and for simplicity, we shall assume that the local model of biasing at quadratic order is the correct underlying bias model. Non-linear biased density fields of this type may be obtained through the following procedure.

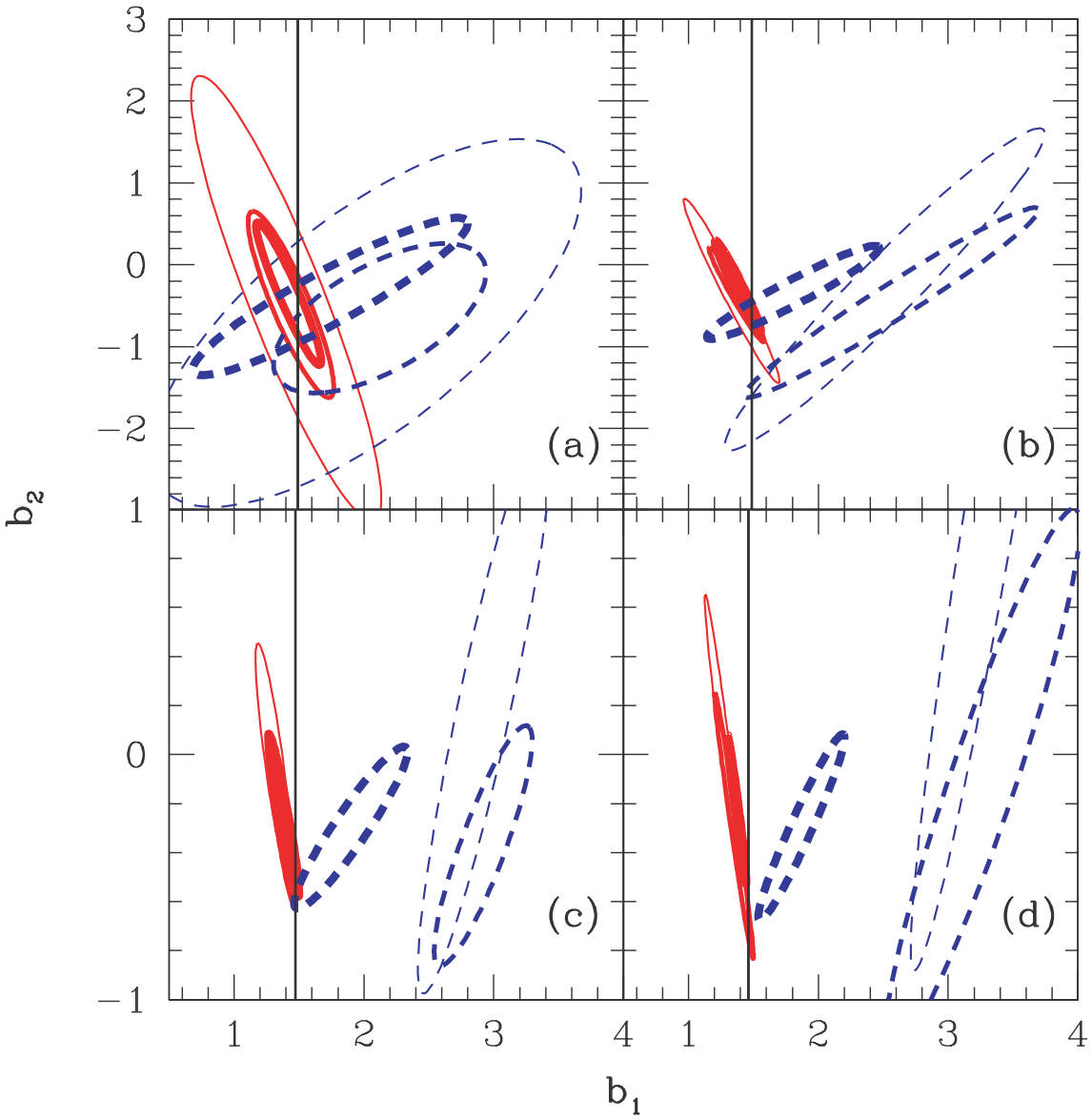

Figure 6. Evolution of the 95 per cent likelihood contours for b_1 and b_2 obtained from the halo auto- and cross-bispectra and reduced bispectra as a function of scale. In each panel, the solid red lines of increasing thickness denote $\{B_{\rm hmm}, B_{\rm hhm}, B_{\rm hhh}\}$ and the dashed blue lines of increasing thickness denote $\{Q_{\rm hmm}, Q_{\rm hhm}, Q_{\rm hhh}\}$. The alphabetical labels {a, b, c, d} correspond to the triangle configurations with $k_1 = \{0.03, 0.04, 0.05, 0.06\}\,h\,{\rm Mpc}^{-1}$, respectively. The vertical black lines denote the effective bias parameter $b_{\rm hh}^{\rm NL,SC}$, using the same wavemodes as that enter into the bispectrum estimates.

For each of the $z = 0$ outputs of the 40 simulations, we assign the non-linear density field of matter to a cubical Fourier grid using the CIC algorithm. This is then Fourier transformed. Each Fourier mode is then smoothed using a Gaussian filter of scale R. We then inverse Fourier transform this field and obtain the smoothed, non-linear matter distribution in real space. Using this we next form the sum

$$\delta_{\rm b}(\boldsymbol{x}|R) = b_1^{\rm b}\delta(\boldsymbol{x}|R) + b_2^{\rm b}[\delta(\boldsymbol{x}|R)]^2/2, \tag{67}$$

where $b_1^{\rm b}$ and $b_2^{\rm b}$ are the artificial bias parameters. Finally, this is Fourier transformed to give us $\delta_{\rm b}(\boldsymbol{k}|R)$. Thus, given $\delta(\boldsymbol{k}|R)$ and $\delta_{\rm b}(\boldsymbol{k}|R)$, we can now use our standard bispectrum estimators to estimate $B_{\rm bbb}$, $B_{\rm bbm}$, $B_{\rm bmm}$ and $B_{\rm mmm}$. We refer to this procedure as the 'biasing-by-hand' test.

The major benefits of these tests are that we are able to better gauge the effects to which non-linearities beyond tree-level order influence the measured bispectra and reduced bispectra. We also note that shot noise plays no role here, since the biased field is created from the matter density field which is densely sampled.

7.2 Theoretical interpretation

In order to interpret the results from such a construction we may use the results presented in Appendix B, with the small modification that we do not de-smooth the results. If we define the smoothed bispectra as

$$\mathcal{B}(\boldsymbol{k}_1, \boldsymbol{k}_2, \boldsymbol{k}_3) \equiv W(k_1R)W(k_2R)W(k_3R)B(\boldsymbol{k}_1, \boldsymbol{k}_2, \boldsymbol{k}_3), \tag{68}$$

then for $\{\mathcal{B}_{\rm bmm},\ \mathcal{B}_{\rm bbm},\ \mathcal{B}_{\rm bbb}\}$, we have

$$\mathcal{B}_{\rm bmm} = b_1\mathcal{B}_{\rm mmm} + \frac{b_2}{6}\mathcal{P}_{4,\rm m}\ , \tag{69}$$

$$\mathcal{B}_{\rm bbm} = b_1^2\mathcal{B}_{\rm mmm} + \frac{b_1 b_2}{3}\mathcal{P}_{4,\rm m} + \frac{b_2^2}{12}\mathcal{P}_{5,\rm m}, \tag{70}$$

$$\mathcal{B}_{\rm bbb} = b_1^3\mathcal{B}_{\rm mmm} + \frac{b_1^2 b_2}{2}\mathcal{P}_{4,\rm m} + \frac{b_1 b_2^2}{4}\mathcal{P}_{5,\rm m} + \frac{b_2^3}{8}\mathcal{P}_{6,\rm m}, \tag{71}$$

where for ease of notation we take $b_i^{\rm b} = b_i$ and in the above we have suppressed the dependence of $\mathcal{B}$, $\mathcal{P}_{4,\rm m}$, $\mathcal{P}_{5,\rm m}$ and $\mathcal{P}_{6,\rm m}$ on $(\boldsymbol{k}_1, \boldsymbol{k}_2, -\boldsymbol{k}_1 - \boldsymbol{k}_2)$. We have also introduced the auxiliary functions

$$\mathcal{P}_{n,\rm m} \equiv W(k_1 R)W(k_2 R)W(k_3 R)P_{n,\rm m}, \tag{72}$$

$$P_{4,\rm m} \equiv \int \frac{{\rm d}^3\boldsymbol{q}_1}{(2\pi)^3}\widetilde{W}_{\boldsymbol{q}_1,\boldsymbol{k}_1-\boldsymbol{q}_1} \times T(\boldsymbol{q}_1, \boldsymbol{k}_1 - \boldsymbol{q}_1, \boldsymbol{k}_2, \boldsymbol{k}_3) + 2\,{\rm cyc}, \tag{73}$$

$$P_{5,\rm m} \equiv \int \frac{{\rm d}^3\boldsymbol{q}_1}{(2\pi)^3}\frac{{\rm d}^3\boldsymbol{q}_2}{(2\pi)^3}\widetilde{W}_{\boldsymbol{q}_1,\boldsymbol{k}_1-\boldsymbol{q}_1}\widetilde{W}_{\boldsymbol{q}_2,\boldsymbol{k}_2-\boldsymbol{q}_2} \times P_{5,\rm m}(\boldsymbol{q}_1, \boldsymbol{k}_1 - \boldsymbol{q}_1, \boldsymbol{q}_2, \boldsymbol{k}_2 - \boldsymbol{q}_2, \boldsymbol{k}_3) + 2\,{\rm cyc}, \tag{74}$$

$$P_{6,\rm m} \equiv \int \frac{{\rm d}^3\boldsymbol{q}_1}{(2\pi)^3}\cdots\frac{{\rm d}^3\boldsymbol{q}_3}{(2\pi)^3}\widetilde{W}_{\boldsymbol{q}_1,\boldsymbol{k}_1-\boldsymbol{q}_1}\cdots\widetilde{W}_{\boldsymbol{q}_3,\boldsymbol{k}_3-\boldsymbol{q}_3} \times P_6(\boldsymbol{q}_1, \boldsymbol{k}_1 - \boldsymbol{q}_1, \boldsymbol{q}_2, \boldsymbol{k}_2 - \boldsymbol{q}_2, \boldsymbol{q}_3, \boldsymbol{k}_3 - \boldsymbol{q}_3). \tag{75}$$

The attractive aspect of this test can now be understood: if we move the terms in equations (69), (70) and (71), which are proportional to $\mathcal{B}_{\rm mmm}$ from the right-hand to the left-hand-side, then we may rewrite this system as the matrix equation

$$\begin{pmatrix} \mathcal{Y}_{\rm bmm} \\ \mathcal{Y}_{\rm bbm} \\ \mathcal{Y}_{\rm bbb} \end{pmatrix} = \begin{pmatrix} b_2/6 & 0 & 0 \\ b_1 b_2/3 & b_2^2/12 & 0 \\ b_1^2 b_2/2 & b_1 b_2^2/4 & b_2^3/8 \end{pmatrix} \begin{pmatrix} \mathcal{P}_{4,\rm m} \\ \mathcal{P}_{5,\rm m} \\ \mathcal{P}_{6,\rm m} \end{pmatrix}, \tag{76}$$

where we defined $\mathcal{Y}_{\rm bmm} \equiv \mathcal{B}_{\rm bmm} - b_1\mathcal{B}_{\rm mmm}$, etc. This equation may be inverted to give

$$\begin{pmatrix} \mathcal{P}_{4,\rm m} \\ \mathcal{P}_{5,\rm m} \\ \mathcal{P}_{6,\rm m} \end{pmatrix} = \frac{1}{b_2^3}\begin{pmatrix} 6b_2^2 & 0 & 0 \\ -24 b_1 b_2 & 12 b_2 & 0 \\ 24 b_1^2 & -24 b_1 & 8 \end{pmatrix} \begin{pmatrix} \mathcal{Y}_{\rm bmm} \\ \mathcal{Y}_{\rm bbm} \\ \mathcal{Y}_{\rm bbb} \end{pmatrix}. \tag{77}$$

Hence, if we specify b_1, b_2 and measure the four bispectra $B_{\rm mmm}$, $B_{\rm bmm}$, $B_{\rm bbm}$ and $B_{\rm bbb}$, then we can exactly determine $\mathcal{P}_{4,\rm m}$, $\mathcal{P}_{5,\rm m}$ and $\mathcal{P}_{6,\rm m}$. Thus, we have complete knowledge of all components of the non-linear model at all orders in the theory. The lowest order PT expansions of these statistics are (cf. Appendix B)

$$\mathcal{B}^{(0)}_{\rm bmm} \approx b_1\mathcal{B}^{(0)}_{\rm mmm} + \frac{b_2}{3}\left[\mathcal{P}^{(0)}_{\rm mm}(k_1)\mathcal{P}^{(0)}_{\rm mm}(k_2) + 2\,{\rm cyc}\right], \tag{78}$$

$$\mathcal{B}^{(0)}_{\rm bbm} \approx b_1^2\mathcal{B}^{(0)}_{\rm mmm} + \frac{b_1 b_2}{3}\left[\mathcal{P}^{(0)}_{\rm mm}(k_1)\mathcal{P}^{(0)}_{\rm mm}(k_2) + 2\,{\rm cyc}\right], \tag{79}$$

$$\mathcal{B}^{(0)}_{\rm bbb} \approx b_1^3\mathcal{B}^{(0)}_{\rm mmm} + b_1^2 b_2\left[\mathcal{P}^{(0)}_{\rm mm}(k_1)\mathcal{P}^{(0)}_{\rm mm}(k_2) + 2\,{\rm cyc}\right], \tag{80}$$

where in the above, we defined $\mathcal{P}_{\rm mm}(k) \equiv W^2(k|R)P_{\rm mm}(k)$.

7.3 Results of the artificial bias test

Following the algorithm described in Section 7.1, for each realization of our ensemble of simulations, we generate three artificially biased density fields smoothed on scales $R = \{20\,, 10\,, 6.67\}\,h^{-1}$ Mpc. In all cases, we apply the same non-linear bias: $b_1 = 1.63$ and $b_2 = -0.53$. Whilst these values are somewhat arbitrary, they were selected to coincide with the best-fitting values to the scatter plot of $\delta_{\rm h}(\boldsymbol{x}|R)$ versus $\delta(\boldsymbol{x}|R)$, smoothed at $R \sim 10\ h^{-1}$ Mpc, that we recorded in Section 4.1.

For each filtering scale, we then measure the four bispectra $B_{\rm mmm}$, $B_{\rm bmm}$, $B_{\rm bbm}$ and $B_{\rm bbb}$ for triangle configurations with $k_1 = 0.04\,h\,{\rm Mpc}^{-1}$, $k_2/k_1 = 2$, over 20 angular bins. From these, using the method described above, we recover the higher order terms: $\mathcal{P}_{4,\rm m}$, $\mathcal{P}_{5,\rm m}$ and $\mathcal{P}_{6,\rm m}$.

We now define three modelling cases of interest:

(i) *Case 1* (*All Order*). Equations (69)–(71) are used to interpret the data.

(ii) *Case 2* (*Exact Trispectrum*). Equations (69)–(71) are exact up to $\mathcal{P}_{4,\rm m}$. All higher order terms ($\mathcal{P}_{5,\rm m}$, $\mathcal{P}_{6,\rm m}$) are dropped from the modelling.

(iii) *Case 3* (*Tree Level*). Lowest order expansions given by equations (78)–(80) are used to interpret the data.

For each of the models described above, we then apply the same χ^2-fitting analysis, as described in Section 5.2, to determine the best-fitting b_1 and b_2 parameters.

We begin by first examining the All Order expansion model. We confirm that for this case, the true bias parameters $b_1 = 1.63$ and $b_2 = -0.53$ are recovered exactly, albeit with some uncertainty, however, with a $\chi^2 = 0$, and for all the smoothing lengths considered. This null test is important, because it gives us confidence that any departures of the fits from the true bias values can be attributed solely to a breakdown of the theoretical modelling.

Next, we focus on the Exact Trispectrum model where $\mathcal{B}_{\rm mmm}$ and $\mathcal{P}_{4,\rm m}$ are measured from the simulations. In Table 7, we report the best-fitting bias parameters with the 1σ errors expressed in quadrature for the auto-bispectrum and cross-bispectrum and for the four smoothing scales examined. For the case $\mathcal{B}_{\rm bmm}$, a quick inspection of equation (69) tells us that the modelling should be exact, and indeed we see that the bias parameters are correctly recovered. However, for the cases $\mathcal{B}_{\rm bbm}$ and $\mathcal{B}_{\rm bbb}$, we see that the absence of the higher order terms ($\mathcal{P}_{5,\rm m}$, $\mathcal{P}_{6,\rm m}$) induces biases in the parameters. For b_1 the deviation from the true value is relatively small, with the value of the parameter only slightly decreasing in size. For b_2 the deviations are larger, and this parameter becomes more positive. We also note that the deviations from the true values appear to increase as the smoothing scale is decreased.

Table 7. Constraints on b_1 and b_2 obtained using the Exact Trispectrum model described in the text. The actual input bias parameters were $b_1 = 1.63$ and $b_2 = -0.53$. Column (1): the smoothing scale of the biased density field; column (2): measured quantity; column (3) and (4): best-fitting values for b_1 and b_2 along with 1σ errors; column (5): the median χ^2.

$R\,(h^{-1}\,{\rm Mpc})$		$b_1 \pm \sigma_{b_1}$	$b_2 \pm \sigma_{b_2}$	χ^2
20	$B_{\rm bbb}$	1.62 ± 0.07	-0.46 ± 0.14	0.01
20	$B_{\rm bbm}$	1.62 ± 0.10	-0.49 ± 0.22	0.00
20	$B_{\rm bmm}$	1.63 ± 0.22	-0.53 ± 0.51	0.00
10	$B_{\rm bbb}$	1.62 ± 0.04	-0.42 ± 0.06	0.15
10	$B_{\rm bbm}$	1.62 ± 0.06	-0.47 ± 0.09	0.02
10	$B_{\rm bmm}$	1.63 ± 0.13	-0.53 ± 0.20	0.00
6.7	$B_{\rm bbb}$	1.59 ± 0.04	-0.35 ± 0.02	0.70
6.7	$B_{\rm bbm}$	1.60 ± 0.05	-0.42 ± 0.04	0.14
6.7	$B_{\rm bmm}$	1.63 ± 0.12	-0.53 ± 0.12	0.00

Table 8. Same as Table 7, but this time the χ^2 analysis is for the tree-level model described in the text.

$R\,(h^{-1}\,\mathrm{Mpc})$		$b_1 \pm \sigma_{b_1}$	$b_2 \pm \sigma_{b_2}$	χ^2
20	B_{bbb}	1.63 ± 0.11	-0.67 ± 0.36	14.75
20	B_{bbm}	1.58 ± 0.17	-0.45 ± 0.65	15.71
20	B_{bmm}	1.37 ± 0.33	0.56 ± 1.19	18.43
10	B_{bbb}	1.49 ± 0.03	-0.66 ± 0.08	13.32
10	B_{bbm}	1.48 ± 0.04	-0.69 ± 0.13	13.60
10	B_{bmm}	1.46 ± 0.09	-0.69 ± 0.29	14.13
6.7	B_{bbb}	1.36 ± 0.02	-0.74 ± 0.06	13.21
6.7	B_{bbm}	1.36 ± 0.03	-0.82 ± 0.09	12.87
6.7	B_{bmm}	1.32 ± 0.07	-0.86 ± 0.22	13.13

Finally, we focus on the tree-level model. Table 8 presents the best-fitting results for b_1 and b_2. We see that in nearly all cases, there are systematic biases in the recovery of the non-linear bias parameters for all of the measured bispectra. In particular, for the case of $\mathcal{B}_{\mathrm{bmm}}$, the results are most deviant and poorly constrained, whereas for $\mathcal{B}_{\mathrm{bbb}}$, only when the data have been smoothed on scales $R = 20\,h^{-1}\,\mathrm{Mpc}$ are the recovered parameters close to the true values.

The comparison of the results from this analysis led us to conclude that the recovered bias parameters are very sensitive to the inclusion of beyond-leading-order corrections in the modelling. Furthermore, accurate non-linear modelling of, at the very least, the matter bispectrum and trispectrum will be essential, if we are to safely recover the non-linear bias parameters from this approach.

8 DISCUSSION

We have evaluated the local halo bias model at second order using three different probes: smoothed density fields; power spectra; and bispectra and reduced bispectra. A summary of our results for the best-fitting bias parameters determined from shot-noise-corrected spectra is shown in Fig. 7.

In the figure, we also compare our estimates for b_1 and b_2 with the analytical predictions for the halo bias parameters obtained from the peak background split (PBS) ansatz (Bardeen et al. 1986; Mo & White 1996). The average theory bias parameters are obtained through computing the expressions

$$\bar{b}_i = \frac{1}{\bar{n}} \int_{M_{\mathrm{min}}}^{\infty} \mathrm{d}M\, n(M)\, b_i(M)\,, \quad \bar{n} \equiv \int_{M_{\mathrm{min}}}^{\infty} \mathrm{d}M\, n(M), \tag{81}$$

where $n(M)$ is the halo mass function, and M_{min} is set equal to the value of the minimum halo mass identified in the simulations (see Section 3). We evaluate the above integral using three different fits to N-body simulations by Sheth & Tormen (1999), Warren et al. (2006) and Pillepich et al. (2010). The corresponding expressions for the bias parameters as a function of halo mass are presented in Scoccimarro et al. (2001b) and Manera et al. (2010).

Considering the results for b_1 (bottom panel), we see that when the reduced bispectra, Q_{hhh}, Q_{hhm} and Q_{hmm}, are used, the recovered parameters are poorly constrained and appear incompatible with respect to the other estimates and are only weakly consistent with one another. On the other hand, the estimates from the bispectra B_{hhh}, B_{hhm} and B_{hmm} are in much better agreement with each other. They are also in close agreement with the predictions from Warren et al. (2006) and Pillepich et al. (2010), which both provided an estimate of $b_1 = 1.39$. However, they slightly undershoot the values from the effective bias estimates, $b_{\mathrm{hh}}^{\mathrm{NL}}$ and $b_{\mathrm{hh}}^{\mathrm{L}}$, likewise the smoothed density fields, and the Sheth–Tormen prediction. The analytical predictions

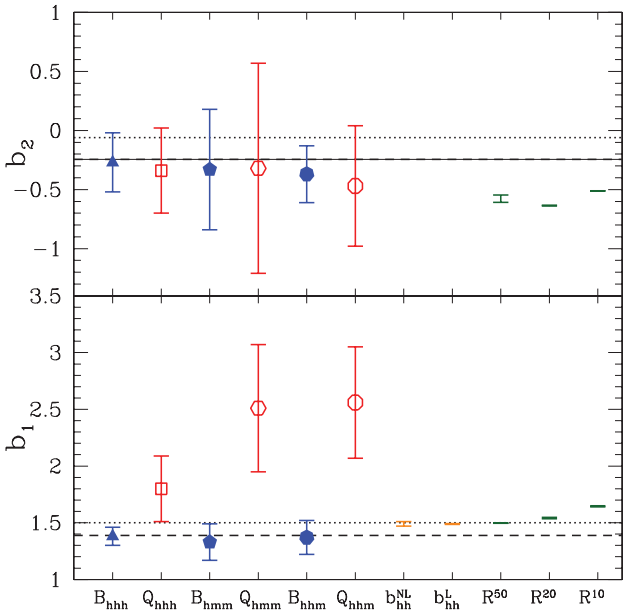

Figure 7. Plot summary of bias measurements on b_1 and b_2 for the second-order local bias model from different estimators: shot-noise-corrected B, Q, P, and finally smoothed, δ^R, in comparison with analytical predictions applying the PBS ansatz with the Sheth & Tormen (1999) mass function denoted by the dotted line, as well as the Warren et al. (2006) and Pillepich et al. (2010) mass functions both of which are represented by the dashed line.

from the Sheth & Tormen (1999) mass function yielded $b_1 = 1.50$ in good agreement with the power spectrum and density field results smoothed on a scale $R \sim 50\,h^{-1}\,\mathrm{Mpc}$. The recovered values of b_1 from the effective bias in the power spectra and the smoothed density fields collectively are in broad agreement, but the latter increase with decreasing smoothing scale.

In the top panel of the figure, we see that the constraints on b_2 from the different estimators used in the simulations are reasonably consistent with one another, albeit with significant error bars. These estimates also agree well with the PBS prediction from the Warren et al. (2006) and Pillepich et al. (2010) mass functions, which give an average $b_2 = -0.24$. However, the prediction from the Sheth & Tormen (1999) mass function gives $b_2 = -0.06$, and this appears to be in worse agreement with the data.

There are a number of possible explanations for the deviations in the recovered bias parameters. First, the relation between matter and halo fluctuations may not be local. Indeed, we know it is not deterministic owing to the scatter in the δ_{h}–δ relation. Perhaps, this is a consequence of non-locality. In this case, we need a more advanced theoretical approach to understand the halo clustering. One possibility may be that the bias is local in Lagrangian space (Catelan et al. 2000; Matsubara 2011).

Secondly, our simple biasing-by-hand test has enabled us to discern that, for the current set of tests that we have performed, the most likely explanation at this point is that the tree-level expansions for B_{hhh} and Q_{hhh} are not sufficiently accurate enough. Higher order non-linear corrections in the modelling must be included, and if possible all order expansions for B_{mmm} and $P_{4,\mathrm{m}}$ would be invaluable.

Thirdly, as we have argued, the local bias model only makes sense in the context of smoothing. The bias parameters one recovers from fitting depend sensitively on the smoothing scale R. For the biasing-by-hand tests, the exact smoothing scale was known beforehand.

However, in real data, we do not know this a priori. In all of the cases, when recovering bias parameters from the bispectra, we have assumed that we are on sufficiently large scales such that $W(k_i R) \rightarrow 1$. However, in general, R should be a free parameter and as such marginalized over in the analysis.

Manera & Gaztañaga (2011) performed a similar study of non-linear halo bias with the three-point correlation function in configuration space. In contrast to our analysis, they measured the bias parameters for different halo mass bins. They found inconsistencies between the predictions of the different estimators considered. They evaluated the scatter plots of $\delta_{\rm h}$ versus δ as a function of smoothing scale, and found that stability in the local bias parameters (b_1, b_2) occurred for smoothing scales, $R > 30$–$60\ h^{-1}\,{\rm Mpc}$, albeit with larger errors. They also found that the bias predictions derived from $\delta_{\rm h}$ versus δ for $R = 60\ h^{-1}\,{\rm Mpc}$ were in good agreement, to within the errors, with the linear bias measured from evaluating the two-point correlation function on large and intermediate scales. As in the case of our findings, they found the linear bias measured from evaluating the three-point correlation function, expressed in terms of the Q amplitudes, was not consistent with that of the two-point correlation function for the lower mass bins: $M < 10^{13}\,h^{-1}\,{\rm M}_{\odot}$. They were unable to formulate solid conclusions for larger mass ranges.

Guo & Jing (2009) explored the differences between estimates of bias from Q and P. They also found that b_1 based on analysis of the mock galaxy catalogues was larger for galaxy-reduced bispectra and power spectra $Q_{\rm g}$ than for $P_{\rm g}$. While Guo & Jing (2009) also noted that this might be due to the failure of SPT at tree level, they also reported that agreement could be found between estimators if $Q_{\rm mmm}$ measured directly from the simulations was used in place of the tree-level expression. However, when we performed the same test with our data we found no dramatic reconciliation of the two bias estimates. The investigation performed by Guo & Jing (2009) was carried out using only four large volume and three smaller volume runs. As a result of having too few realizations, they assumed the Gaussian approximation for the covariance matrix in order to perform their study at large scales.

9 CONCLUSIONS

In this paper, we have used a sample of 40 large-volume N-body simulations, with total volume $V \sim 135\,{\rm Gpc}^3\,h^{-3}$, to test the local model of halo biasing, and the extent to which non-linearities impact the modelling. We used three different methods for exploring the bias: smoothed density fields; power spectra; and bispectra and reduced bispectra. We focused mainly on the results from the bispectra. All of the reported results were scaled to a single realization of our simulations, and so are directly relevant for galaxy surveys with a total volume $V \sim 4\,h^{-3}\,{\rm Gpc}^3$.

In Section 2, we reviewed the basic results of PT and how they connect to density statistics. We then reviewed the local model of halo biasing, drawing special attention to the role that smoothing plays in the theory. The important result being that even at tree level the smoothing explicitly enters the theory. The expressions for $B_{\rm hhh}$ and $Q_{\rm hhh}$, which are typically used in all past and current analyses, make the assumption that smoothing is unimportant. In subsequent sections, we argued that this assumption is not safe.

In Section 3, we described our suite of N-body simulations, and the halo catalogues used in this study.

In Section 4, we made measurements of the relation between $\delta_{\rm h}(\boldsymbol{x}|R)$ and $\delta(\boldsymbol{x}|R)$ smoothed on the set of scales $R = \{50,\ 20,\ 10\}\ h^{-1}\,{\rm Mpc}$. To these data we fitted the local model of halo biasing up to second order, including b_0, b_1 and b_2. We found that the fits were reasonably good; however, the best-fitting parameters showed a running with the filter scale R. We then demonstrated, theoretically, why the non-linear bias parameters from this approach could not be made independent of smoothing scale. We then turned to Fourier-space statistics, and used the halo auto- and cross-power spectra to obtain an effective large-scale bias. We found that the effective bias estimators $b_{\rm hh}^{\rm NL}$ and $b_{\rm hm}^{\rm NL}$ were reasonably scale-independent for $k < 0.08\,h\,{\rm Mpc}^{-1}$. However, on scales smaller than this, $b_{\rm hh}^{\rm NL}$ decreased with increasing wavenumber, whereas $b_{\rm hm}^{\rm NL}$ remained surprisingly flat.

In Section 5, we estimated the matter auto- and halo auto-bispectra and reduced bispectra from our simulations. We measured these statistics for the triangle configurations $k_1 = \{0.03, 0.04, 0.05, 0.06\}\,h\,{\rm Mpc}^{-1}$ and with $k_2/k_1 = 2$ and $\theta_{12} \in [0, \pi]$. These triangles all lie in the weakly non-linear regime $k = 0.03$–$0.18\ h\,{\rm Mpc}^{-1}$. We modelled these estimates using tree-level PT expressions for the matter bispectrum and non-linear bias at second order, and assumed smoothing to be unimportant. Our method for the estimation of the bias parameters followed a standard minimum χ^2 approach. We estimated the covariance matrix for the full ensemble applying PCA to minimize the intrinsic noise. We also performed a jackknife subsampling routine to propagate the error of the estimated covariance matrix on to the errors of the bias parameters.

We tested how well the measurements of the matter bispectra $B_{\rm mmm}$ and reduced bispectra $Q_{\rm mmm}$ could be described by such modelling. The results obtained for the bias parameters b_1 and b_2 showed that the tree-level expressions were a good description of the data for configurations, $k_1 = \{0.03, 0.04\}\,h\,{\rm Mpc}^{-1}$, for which $b_1 = 1$ and $b_2 = 0$. However, for smaller scale triangles, $k_1 = \{0.05, 0.06\}\,h\,{\rm Mpc}^{-1}$, significant deviations were apparent, and these were manifested as $b_1 \neq 1$ and $b_2 \neq 0$ at high significance.

We then applied the χ^2 test to the halo bispectra $B_{\rm hhh}$ and reduced bispectra $Q_{\rm hhh}$. We found, for the shot-noise-corrected $B_{\rm hhh}$, that the estimated values for $b_1 \sim 1.40$ and $b_2 \sim -0.25$ were reasonably consistent with one another. However, the fits became progressively poorer as smaller scales were added, yet the reduced χ^2 remained $\lesssim 2$ for $k_1 = \{0.06\}\,h\,{\rm Mpc}^{-1}$. For the shot-noise-corrected $Q_{\rm hhh}$, we found that the values of b_1 were significantly larger, $b_1 \sim 1.85$, with large errors, and the values evolved with triangle configuration scale. However, $b_2 \sim -0.3$ appeared to be more stable, although again with large errors. For triangle configurations with $k_1 \geq 0.04\,h\,{\rm Mpc}^{-1}$, the fits from $B_{\rm hhh}$ and $Q_{\rm hhh}$ were inconsistent with each other at the $\sim 3\sigma$ level. For both $B_{\rm hhh}$ and $Q_{\rm hhh}$, shot-noise corrections significantly influenced the recovered bias parameters.

In Section 6, we explored the halo and matter cross-bispectra, $B_{\rm hhm}$ and $B_{\rm hmm}$, and reduced bispectra $Q_{\rm hhm}$ and $Q_{\rm hmm}$. We calculated the tree-level expressions for these quantities symmetrized in all of their arguments. We then developed estimators for them. We showed that for $B_{\rm hmm}$ and $Q_{\rm hmm}$, provided the matter distribution was densely sampled, the shot-noise corrections were small.

We applied the χ^2 analysis from Section 5 to these statistics and recovered the best-fitting values for b_1 and b_2. We found that for $B_{\rm hhm}$ the shot-noise-corrected data were all reasonably consistent with one another, giving $b_1 \sim 1.39$ and $b_2 \sim -0.3$. For $B_{\rm hmm}$ we found a similar pattern, except that for $k_1 \geq 0.05\,h\,{\rm Mpc}^{-1}$ where we found $b_2 \sim 0.0$, but with large errors. The results for $Q_{\rm hhm}$ and $Q_{\rm hmm}$ appeared to vary significantly.

Finally, in Section 7, we explored to what extent the breakdown could be attributed to the absence of terms that were beyond tree

level in the modelling. In order to do this, we developed a novel approach, whereby we constructed smoothed biased density fields from the smoothed matter density field, using the local model at quadratic order. We showed that if we set b_1 and b_2 to some fiducial values, and then measure the smoothed matter and halo bispectra and their cross-bispectra, then the higher order matter correlators $P_{4,\mathrm{m}}$, $P_{5,\mathrm{m}}$ and $P_{6,\mathrm{m}}$ could be recovered exactly. Thus, we were able to construct three models: an all order model; a model that used the exact matter bispectrum and trispectrum; and a tree-level model.

We applied the χ^2 analysis using these three models and for bispectra with $k_1 = 0.04\,h\,\mathrm{Mpc}^{-1}$. As expected, the exact model recovered the correct bias parameters. The model with the exact B_{mmm} and $P_{4,\mathrm{m}}$ was in fact also exact for B_{bmm}. For B_{bbm} and B_{bbb} the recovered parameters were close to the true values, but showed evolution with smoothing scale. Finally, for the tree-level model we showed that there was a significant evolution in the estimated bias parameters with smoothing scale and with the type of statistic used.

We conclude that estimates of non-linear bias from the bispectrum that do not attempt to account for higher order corrections will most likely provide biased estimates for the bias parameters b_1 and b_2. Robust modelling of non-linear bias from bispectra will, at the very least, require almost exact models for the matter bispectrum and trispectrum.

Real-space estimates of bias appear to be inconsistent with Fourier-space-based ones. We believe that this owes primarily to the mixing of large- and small-scale wavemodes in real space. We therefore recommend that perturbative methods should strictly be applied in Fourier space. We also recommend that measurements focus on the bispectrum and the associated cross-statistics, rather than the reduced bispectra, since this appears very sensitive to non-linearities in the modelling and also shot-noise corrections.

Finally, we emphasize the importance of smoothing in the local model. Owing to the fact that the smoothing scale associated with the halo/galaxy distribution in question is not known a priori, it must be treated as a nuisance parameter and so marginalized over.

An alternative strategy for recovering information from higher order statistics, which may be of interest for future consideration, is the use of 'Gaussianizing transformations' or 'density clipping' (Neyrinck, Szapudi & Szalay 2009; Seo et al. 2011; Simpson et al. 2011). However, the theoretical connection between what is measured and what is interpreted from such approaches still remains to be fully calculated.

ACKNOWLEDGMENTS

We thank the anonymous referee for helpful suggestions. We also thank Tobias Baldauf, Martin Crocce, Roman Scoccimarro, Emiliano Sefussati, Ravi Sheth and Masahiro Takada for useful discussions. We thank V. Springel for making public GADGET-2 and for providing his B-FOF halo finder, and R. Scoccimarro for making public his 2LPT code. JEP and CP were supported by funding provided through the SFB-Transregio 33 The Dark Universe by the Deutsche Forschungsgemeinschaft. RES acknowledges support from a Marie Curie Reintegration Grant, the Alexander von Humboldt Foundation and partial support from the Swiss National Foundation under contract 200021-116696/1.

REFERENCES

Baldauf T., Seljak U., Senatore L., 2011, J. Cosmol. Astropart. Phys., 4, 6
Bardeen J. M., Bond J. R., Kaiser N., Szalay A. S., 1986, ApJ, 304, 15
Bernardeau F., Colombi S., Gaztañaga E., Scoccimarro R., 2002, Phys. Rep., 367, 1
Bouchet F. R., Colombi S., Hivon E., Juszkiewicz R., 1995, A&A, 296, 575
Catelan P., Porciani C., Kamionkowski M., 2000, MNRAS, 318, L39
Coles P., 1993, MNRAS, 262, 1065
Crocce M., Pueblas S., Scoccimarro R., 2006, MNRAS, 373, 369
Dalal N., Doré O., Huterer D., Shirokov A., 2008, Phys. Rev. D, 77, 123514
Davis M., Efstathiou G., Frenk C. S., White S. D. M., 1985, ApJ, 292, 371
Dekel A., Lahav O., 1999, ApJ, 520, 24
Dekel A., Rees M. J., 1987, Nat, 326, 455
Desjacques V., Seljak U., Iliev I. T., 2009, MNRAS, 396, 85
Feldman H. A., Frieman J. A., Fry J. N., Scoccimarro R., 2001, Phys. Rev. Lett., 86, 1434
Fry J. N., 1994, ApJ, 421, 21
Fry J. N., Gaztanaga E., 1993, ApJ, 413, 447
Fry J. N., Scherrer R. J., 1994, ApJ, 429, 36
Gaztañaga E., Scoccimarro R., 2005, MNRAS, 361, 824
Gaztañaga E., Norberg P., Baugh C. M., Croton D. J., 2005, MNRAS, 364, 620
Goroff M. H., Grinstein B., Rey S.-J., Wise M. B., 1986, ApJ, 311, 6
Guo H., Jing Y. P., 2009, ApJ, 702, 425
Guzik J., Bernstein G., Smith R. E., 2007, MNRAS, 375, 1329
Hartlap J., Simon P., Schneider P., 2007, A&A, 464, 399
Heavens A. F., Matarrese S., Verde L., 1998, MNRAS, 301, 797
Hivon E., Bouchet F. R., Colombi S., Juszkiewicz R., 1995, A&A, 298, 643
Hockney R. W., Eastwood J. W., 1988, Computer Simulation Using Particles. Hilger, Bristol
Jain B., Bertschinger E., 1994, ApJ, 431, 495
Jing Y. P., 2005, ApJ, 620, 559
Joachimi B., Shi X., Schneider P., 2009, A&A, 508, 1193
Juszkiewicz R., 1981, MNRAS, 197, 931
Kaiser N., 1984, ApJ, 284, L9
Komatsu E. et al., 2009, ApJS, 180, 330
Komatsu E. et al. (The WMAP Team), 2011, ApJS, 192, 18
McBride C. K., Connolly A. J., Gardner J. P., Scranton R., Newman J. A., Scoccimarro R., Zehavi I., Schneider D. P., 2011, ApJ, 726, 13
Makino N., Sasaki M., Suto Y., 1992, Phys. Rev. D, 46, 585
Manera M., Gaztañaga E., 2011, MNRAS, 415, 383
Manera M., Sheth R. K., Scoccimarro R., 2010, MNRAS, 402, 589
Marin F., 2011, ApJ, 737, 97
Matarrese S., Verde L., Heavens A. F., 1997, MNRAS, 290, 651
Matsubara T., 2011, Phys. Rev. D, 83, 083518
Mo H. J., White S. D. M., 1996, MNRAS, 282, 347
Mo H. J., Jing Y. P., White S. D. M., 1997, MNRAS, 284, 189
Neyrinck M. C., Szapudi I., Szalay A. S., 2009, ApJ, 698, L90
Nishimichi T. et al., 2007, PASJ, 59, 1049
Nishimichi T., Taruya A., Koyama K., Sabiu C., 2010, J. Cosmol. Astropart. Phys., 7, 2
Norberg P., Baugh C. M., Gaztañaga E., Croton D. J., 2009, MNRAS, 396, 19
Padmanabhan N., White M., Norberg P., Porciani C., 2009, MNRAS, 397, 1862
Peebles P. J. E., 1980, The Large-scale Structure of the Universe. Princeton Univ. Press, Princeton, NJ
Peebles P. J. E., Groth E. J., 1975, ApJ, 196, 1
Pillepich A., Porciani C., Hahn O., 2010, MNRAS, 402, 191
Porciani C., Giavalisco M., 2002, ApJ, 565, 24
Roth N., Porciani C., 2011, MNRAS, 415, 829
Scoccimarro R., 1998, MNRAS, 299, 1097
Scoccimarro R., 2000, ApJ, 544, 597
Scoccimarro R., Colombi S., Fry J. N., Frieman J. A., Hivon E., Melott A., 1998, ApJ, 496, 586
Scoccimarro R., Couchman H. M. P., Frieman J. A., 1999, ApJ, 517, 531
Scoccimarro R., Feldman H. A., Fry J. N., Frieman J. A., 2001a, ApJ, 546, 652
Scoccimarro R., Sheth R. K., Hui L., Jain B., 2001b, ApJ, 546, 20
Sefusatti E., 2009, Phys. Rev. D, 80, 123002
Sefusatti E., Komatsu E., 2007, Phys. Rev. D, 76, 083004

Sefusatti E., Crocce M., Pueblas S., Scoccimarro R., 2006, Phys. Rev. D, 74, 023522
Seljak U., Zaldarriaga M., 1996, ApJ, 469, 437
Seljak U., Sugiyama N., White M., Zaldarriaga M., 2003, Phys. Rev. D, 68, 083507
Seo H.-J., Sato M., Dodelson S., Jain B., Takada M., 2011, ApJ, 729, L11
Sheth R. K., Lemson G., 1999, MNRAS, 304, 767
Sheth R. K., Tormen G., 1999, MNRAS, 308, 119
Simpson F., Berian James J., Heavens A. F., Heymans C., 2011, Phys. Rev. Lett., 107, 271301
Smith R. E., 2009, MNRAS, 400, 851
Smith R. E., Marian L., 2011, MNRAS, 418, 729
Smith R. E., Scoccimarro R., Sheth R. K., 2007, Phys. Rev. D, 75, 063512
Smith R. E., Sheth R. K., Scoccimarro R., 2008, Phys. Rev. D, 78, 023523
Smith R. E., Hernández-Monteagudo C., Seljak U., 2009, Phys. Rev. D, 80, 063528
Springel V., 2005, MNRAS, 364, 1105
Verde L. et al. (The 2dFGRS Team), 2002, MNRAS, 335, 432
Vishniac E. T., 1983, MNRAS, 203, 345
Warren M. S., Abazajian K., Holz D. E., Teodoro L., 2006, ApJ, 646, 881
White S. D. M., Rees M. J., 1978, MNRAS, 183, 341

APPENDIX A: BISPECTRUM ESTIMATION: ALGORITHM

Briefly, the algorithm that we employ is as follows: first, the dark matter density field is computed by assigning the dark matter particles to a cubical grid using the CIC technique (Hockney & Eastwood 1988). Next, the FFT of the gridded density field is computed. Each Fourier mode is then corrected for convolution with the Fourier mesh. We do this by dividing out from each mode the Fourier transform of the window assignment function of the CIC scheme (Hockney & Eastwood 1988; Jing 2005):

$$\delta(\boldsymbol{k}) = \frac{\delta_{\rm g}(\boldsymbol{k})}{W_{\rm CIC}(\boldsymbol{k})}\ ;\ \ W_{\rm CIC}(\boldsymbol{k}) \equiv \prod_{i=1,3}\left[\frac{\sin(\pi k_i/2k_{\rm Ny})}{\pi k_i/2k_{\rm Ny}}\right]^2, \tag{A1}$$

where the subscript g denotes gridded quantities, $k_{\rm Ny} = \pi N_{\rm g}/L$ is the Nyquist frequency of the mesh and $N_{\rm g}$ is the number of Fourier grid cells.

The estimator for the bispectrum can be written (Scoccimarro et al. 1998) as

$$\widehat{B}(k_1, k_2, \theta) = \frac{V_\mu^2}{V_B(k_1, k_2, \theta)} \int \frac{{\rm d}^3\boldsymbol{q}_1}{(2\pi)^3}\frac{{\rm d}^3\boldsymbol{q}_2}{(2\pi)^3}\frac{{\rm d}^3\boldsymbol{q}_3}{(2\pi)^3}(2\pi)^3\delta^{\rm D}(\boldsymbol{q}_{123})\delta(\boldsymbol{q}_1)\delta(\boldsymbol{q}_2)\delta(\boldsymbol{q}_3), \tag{A2}$$

where V_μ is the sample volume (in our case the simulation volume), the normalization factor, V_B, can be written as (Sefusatti et al. 2006; Joachimi, Shi & Schneider 2009)

$$V_B(k_1, k_2, \mu) \equiv \int \frac{{\rm d}^3\boldsymbol{q}_1}{(2\pi)^3}\frac{{\rm d}^3\boldsymbol{q}_2}{(2\pi)^3}\frac{{\rm d}^3\boldsymbol{q}_3}{(2\pi)^3}(2\pi)^3\delta^{\rm D}(\boldsymbol{q}_{123}) \approx \frac{8\pi^2 k_1 k_2 k_3}{(2\pi)^6}(\Delta k)^3, \tag{A3}$$

and we write in shorthand $\delta^{\rm D}(\boldsymbol{q}_{1\ldots n}) \equiv \delta^{\rm D}(\boldsymbol{q}_1 + \cdots + \boldsymbol{q}_n)$. A practical implementation of the above estimator may be achieved through (Smith et al. 2008)

$$\widehat{B}^{\rm d}(k_1, k_2, \theta_{12}) = \frac{V_\mu^2}{N_{\rm tri}(k_1, k_2, \theta_{12})} \sum_{(\boldsymbol{n}_1, \boldsymbol{n}_2)}^{N_{\rm tri}(k_1, k_2, \theta_{12})} \mathcal{R}e[\delta(\boldsymbol{k}_{\boldsymbol{n}_1})\delta(\boldsymbol{k}_{\boldsymbol{n}_2})\delta(\boldsymbol{k}_{-\boldsymbol{n}_1-\boldsymbol{n}_2})], \tag{A4}$$

where the superscript 'd' denotes discretized quantities; $\boldsymbol{n}_i$ denotes an integer vector from the origin of the k space to each mesh point; $(\boldsymbol{n}_1, \boldsymbol{n}_2)$ represents a pair of integer vectors that lie in thin shells centred on k_1 and k_2 and whose angular separation lies in a narrow angular bin centred on θ_{12}, and for which $\boldsymbol{k}_3 = -\boldsymbol{k}_1 - \boldsymbol{k}_2$. The upper limit of the sum $N_{\rm tri}(k_1, k_2, \theta_{12})$ represents the total number of triangles that have such a configuration.

The estimator for the bin-averaged reduced bispectrum, $\widehat{Q}$, is written as

$$\widehat{Q}^{\rm d} = \widehat{B}^{\rm d}/\widehat{Q}^{\rm denom,d}, \tag{A5}$$

where $\widehat{Q}^{\rm denom,d}$ is the estimator for the bin-averaged cyclical terms of the power spectrum generated from first computing the bin-averaged power spectra, $\widehat{P}_i^{\rm d}$. Note that we estimate the power spectra that enter into this product in a slightly different way from normal: we use only those modes that go into estimating the particular B triangle configuration to estimate $\widehat{Q}^{\rm denom,d}(k_1, k_2, \theta_{12})$. Hence,

$$\widehat{P}_i^{\rm d} = \frac{V_\mu}{N_{\rm tri}(k_1, k_2, \theta_{12})} \sum_{(\boldsymbol{n}_1, \boldsymbol{n}_2)}^{N_{\rm tri}(k_1, k_2, \theta_{12})} |\delta(\boldsymbol{k}_{\boldsymbol{n}_i})|^2, \tag{A6}$$

where $i \in \{1, 2, 3\}$ and $\widehat{P}_3^{\rm d}$ is dependent on the angular bin, since, with $|\boldsymbol{n}_1|$ and $|\boldsymbol{n}_2|$ fixed, we still have $\cos\theta_{12} = \boldsymbol{n}_1 \cdot \boldsymbol{n}_2/|\boldsymbol{n}_1||\boldsymbol{n}_2|$ and the closure criterion implies $\boldsymbol{n}_3 = -\boldsymbol{n}_1 - \boldsymbol{n}_2$ varies as a function of θ_{12}. Therefore,

$$\widehat{Q}^{\rm denom,d} = \widehat{P}_1^{\rm d}\widehat{P}_2^{\rm d} + \widehat{P}_2^{\rm d}\widehat{P}_3^{\rm d} + \widehat{P}_1^{\rm d}\widehat{P}_3^{\rm d}. \tag{A7}$$

The estimates of $B^{\rm d}$ and $Q^{\rm d}$ are then corrected for discreteness, that is, shot noise. For the estimators of interest, the corrections are (Peebles 1980; Smith et al. 2008)

$$\widehat{P}_{\rm shot} \equiv 1/\overline{n}\ , \tag{A8}$$

$$\widehat{\overline{B}}_{\rm shot} \equiv \left(\widehat{\overline{P}}_1^{\rm d} + \widehat{\overline{P}}_2^{\rm d} + \widehat{\overline{P}}_3^{\rm d}\right)/\overline{n} - 2/\overline{n}^2\,, \tag{A9}$$

$$\widehat{\overline{Q}}_{\rm shot}^{\rm denom} \equiv 2\left(\widehat{\overline{P}}_1^{\rm d} + \widehat{\overline{P}}_2^{\rm d} + \widehat{\overline{P}}_3^{\rm d}\right)/\overline{n} - 3/\overline{n}^2. \tag{A10}$$

Shot-noise-corrected estimates of the statistics are obtained as

$$\chi = \chi^{\rm d} - \chi_{\rm shot}\,, \tag{A11}$$

where $\chi \in \left\{\widehat{\overline{P}}, \widehat{\overline{B}}, \widehat{\overline{Q}}^{\rm denom}\right\}$ and $\widehat{\overline{Q}} = \widehat{\overline{B}}/\widehat{\overline{Q}}^{\rm denom}$. Note that the above recipe corrects some typos that are present in Smith et al. (2008).

APPENDIX B: HALO CROSS-BISPECTRA IN THE LOCAL MODEL

As was shown in equation (15), at quadratic order, the local model of non-linear biasing can be written as

$$\delta_{\rm h}(\boldsymbol{k}|R) = b_1(M)\delta(\boldsymbol{k}|R) + \frac{b_2(M)}{2}\int \frac{{\rm d}^3\boldsymbol{q}_1}{(2\pi)^3}\frac{{\rm d}^3\boldsymbol{q}_1}{(2\pi)^3}\delta(\boldsymbol{q}_1|R)\delta(\boldsymbol{q}_2|R)(2\pi)^3\delta^{\rm D}(\boldsymbol{k}_1 - \boldsymbol{q}_1 - \boldsymbol{q}_2), \tag{B1}$$

where $\delta(\boldsymbol{q}_i|R) \equiv \delta(\boldsymbol{q}_i)W(q_i R)$ is the filtered density. Using this model, we may now proceed to calculate the halo auto- and halo–mass cross-bispectra.

B1 Halo–mass–mass bispectrum in the local model

Let us start with the simplest three-point cross-statistic, the halo–mass–mass bispectrum, which can be written as

$$\begin{aligned}\langle\delta_{\rm h}(\boldsymbol{k}_1|M,R)\delta(\boldsymbol{k}_2|R)\delta(\boldsymbol{k}_3|R)\rangle &= b_1(M)\,\langle\delta(\boldsymbol{k}_1|R)\delta(\boldsymbol{k}_2|R)\delta(\boldsymbol{k}_3|R)\rangle \\ &\quad + \frac{b_2(M)}{2}\int\frac{{\rm d}^3\boldsymbol{q}_1}{(2\pi)^3}\frac{{\rm d}^3\boldsymbol{q}_1}{(2\pi)^3}(2\pi)^3\delta^{\rm D}(\boldsymbol{k}_1-\boldsymbol{q}_1-\boldsymbol{q}_2)\left\langle\delta(\boldsymbol{q}_1|R)\delta(\boldsymbol{q}_2|R)\delta(\boldsymbol{k}_1|R)\delta(\boldsymbol{k}_2|R)\right\rangle.\end{aligned} \tag{B2}$$

Let us define the smoothed n-point spectra as

$$\begin{aligned}\langle\delta(\boldsymbol{k}_1|R)\ldots\delta(\boldsymbol{k}_n|R)\rangle &\equiv (2\pi)^3\delta(\boldsymbol{k}_1+\cdots+\boldsymbol{k}_n)\widetilde{\mathcal{P}}_n(\boldsymbol{k}_1,\ldots,\boldsymbol{k}_n|R), \\ &= (2\pi)^3\delta(\boldsymbol{k}_1+\cdots+\boldsymbol{k}_m)W(k_1R)\ldots W(k_nR)P_n(\boldsymbol{k}_1,\ldots,\boldsymbol{k}_n),\end{aligned} \tag{B3}$$

where $\widetilde{\mathcal{P}}_2 \equiv \widetilde{\mathcal{P}} = W^2(kR)P$, $\widetilde{\mathcal{P}}_3 \equiv \widetilde{\mathcal{B}} = W(k_1R)W(k_2R)W(k_3R)B$, and $\widetilde{\mathcal{P}}_4 \equiv \widetilde{\mathcal{T}} = W(k_1R)W(k_2R)W(k_3R)W(k_4R)T$. We may now integrate over $\boldsymbol{q}_2$ to obtain

$$\langle\delta_{\rm h}(\boldsymbol{k}_1|M,R)\delta(\boldsymbol{k}_2|R)\delta(\boldsymbol{k}_3|R)\rangle = (2\pi)^3\delta^{\rm D}(\boldsymbol{k}_1+\boldsymbol{k}_2+\boldsymbol{k}_3)\left[b_1(M)\widetilde{\mathcal{B}}(\boldsymbol{k}_1,\boldsymbol{k}_2,\boldsymbol{k}_3) + \frac{b_2(M)}{2}\int\frac{{\rm d}^3\boldsymbol{q}_1}{(2\pi)^3}\widetilde{\mathcal{T}}(\boldsymbol{q}_1,\boldsymbol{k}_1-\boldsymbol{q}_1,\boldsymbol{k}_2,\boldsymbol{k}_3)\right]. \tag{B4}$$

On dividing the above expression by $W(k_1R)W(k_2R)W(k_3R)$, the halo–mass–mass bispectrum can be written as

$$B_{\rm hmm}(\boldsymbol{k}_1,\boldsymbol{k}_2,\boldsymbol{k}_3) = b_1(M)B_{\rm mmm}(\boldsymbol{k}_1,\boldsymbol{k}_2,\boldsymbol{k}_3) + \frac{b_2(M)}{2}\int\frac{{\rm d}^3\boldsymbol{q}_1}{(2\pi)^3}\widetilde{W}_{\boldsymbol{q}_1,\boldsymbol{k}_1-\boldsymbol{q}_1}T_{\rm mmmm}(\boldsymbol{q}_1,\boldsymbol{k}_1-\boldsymbol{q}_1,\boldsymbol{k}_2,\boldsymbol{k}_3). \tag{B5}$$

We may symmetrize the above result by constructing the sum $(B_{\rm hmm}+B_{\rm mhm}+B_{\rm mmh})/3$, and this gives us

$$B_{\rm hmm}(\boldsymbol{k}_1,\boldsymbol{k}_2,\boldsymbol{k}_3) = b_1(M)B_{\rm mmm}(\boldsymbol{k}_1,\boldsymbol{k}_2,\boldsymbol{k}_3) + \frac{b_2(M)}{6}\int\frac{{\rm d}^3\boldsymbol{q}_1}{(2\pi)^3}\left[\widetilde{W}_{\boldsymbol{q}_1,\boldsymbol{k}_1-\boldsymbol{q}_1}T_{\rm mmmm}(\boldsymbol{q}_1,\boldsymbol{k}_1-\boldsymbol{q}_1,\boldsymbol{k}_2,\boldsymbol{k}_3) + 2\,{\rm cyc}\right]. \tag{B6}$$

On expanding B and T to fourth order in δ, the above expression can be approximated to

$$B^{(0)}_{\rm hmm}(\boldsymbol{k}_1,\boldsymbol{k}_2,\boldsymbol{k}_3) \approx b_1(M)B^{(0)}_{\rm mmm}(\boldsymbol{k}_1,\boldsymbol{k}_2,\boldsymbol{k}_3) + \frac{b_2(M)}{3}\left[\widetilde{W}_{\boldsymbol{k}_2,\boldsymbol{k}_3}P^{(0)}_{\rm mm}(k_2)P^{(0)}_{\rm mm}(k_3) + 2\,{\rm cyc}\right]. \tag{B7}$$

Finally, in the large-scale limit $k_i \to 0$, or for arbitrarily small smoothing scales, $k_iR \ll 1$, the above expression becomes

$$B^{(0)}_{\rm hmm}(\boldsymbol{k}_1,\boldsymbol{k}_2,\boldsymbol{k}_3) \approx b_1(M)B^{(0)}_{\rm mmm}(\boldsymbol{k}_1,\boldsymbol{k}_2,\boldsymbol{k}_3) + \frac{b_2(M)}{3}\left[P^{(0)}_{\rm mm}(k_2)P^{(0)}_{\rm mm}(k_3) + 2\,{\rm cyc}\right]. \tag{B8}$$

The reduced bispectrum $Q_{\rm hmm}$ is given by

$$Q_{\rm hmm}(\boldsymbol{k}_1,\boldsymbol{k}_2,\boldsymbol{k}_3) \equiv \frac{B_{\rm hmm}(\boldsymbol{k}_1,\boldsymbol{k}_2,\boldsymbol{k}_3)}{P\,P_{\rm hmm}}, \tag{B9}$$

where

$$P\,P_{\rm hmm} = \frac{2}{3}\left[P_{\rm hm}(k_1)P_{\rm mm}(k_2) + 2\,{\rm cyc}\right] + \frac{1}{3}\left[P_{\rm hm}(k_1)P_{\rm hm}(k_2) + 2\,{\rm cyc}\right]. \tag{B10}$$

In order to calculate the reduced halo–mass cross-bispectrum, we need to evaluate the halo–mass power spectrum. In the local model and up to quadratic order in the bias, we have

$$P_{\rm hm}(k) = b_1(M)P_{\rm mm}(\boldsymbol{k}_1) + \frac{b_2(M)}{2}\int\frac{{\rm d}^3\boldsymbol{q}_1}{(2\pi)^3}\widetilde{W}_{\boldsymbol{q}_1,\boldsymbol{k}_1-\boldsymbol{q}_1}B_{\rm mmm}(\boldsymbol{q}_1,\boldsymbol{k}_1-\boldsymbol{q}_1,-\boldsymbol{k}_1). \tag{B11}$$

Using the above expression in equation (B10), we find

$$P P_{\rm hmm}(\boldsymbol{k}_1, \boldsymbol{k}_2, \boldsymbol{k}_3) = \left\{ \frac{2}{3} \left[b_1(M) P_{\rm mm}(\boldsymbol{k}_1) + \frac{b_2(M)}{2} \int \frac{{\rm d}^3\boldsymbol{q}_1}{(2\pi)^3} \widetilde{W}_{\boldsymbol{q}_1, \boldsymbol{k}_1 - \boldsymbol{q}_1} B_{\rm mmm}(\boldsymbol{q}_1, \boldsymbol{k}_1 - \boldsymbol{q}_1, -\boldsymbol{k}_1) \right] P_{\rm mm}(k_2) + 2\,{\rm cyc} \right\}$$
$$+ \frac{1}{3} \left\{ \left[b_1(M) P_{\rm mm}(\boldsymbol{k}_1) + \frac{b_2(M)}{2} \int \frac{{\rm d}^3\boldsymbol{q}_1}{(2\pi)^3} \widetilde{W}_{\boldsymbol{q}_1, \boldsymbol{k}_1 - \boldsymbol{q}_1} B_{\rm mmm}(\boldsymbol{q}_1, \boldsymbol{k}_1 - \boldsymbol{q}_1, -\boldsymbol{k}_1) \right] \right.$$
$$\left. \times \left[b_1(M) P_{\rm mm}(\boldsymbol{k}_2) + \frac{b_2}{2} \int \frac{{\rm d}^3\boldsymbol{q}_1}{(2\pi)^3} \widetilde{W}_{\boldsymbol{q}_2, \boldsymbol{k}_2 - \boldsymbol{q}_2} B_{\rm mmm}(\boldsymbol{q}_2, \boldsymbol{k}_2 - \boldsymbol{q}_2, -\boldsymbol{k}_2) \right] + 2\,{\rm cyc} \right\}. \tag{B12}$$

If we expand $PP_{\rm hmm}$ to fourth order in the density, then the above expression simplifies to

$$P P^{(0)}_{\rm hmm}(\boldsymbol{k}_1, \boldsymbol{k}_2, \boldsymbol{k}_3) \approx \frac{b_1(M)}{3} \left[2 + b_1(M) \right] \left[P^{(0)}_{\rm mm}(k_1) P^{(0)}_{\rm mm}(k_2) + 2\,{\rm cyc} \right]. \tag{B13}$$

Hence, we have

$$Q^{(0)}_{\rm hmm}(\boldsymbol{k}_1, \boldsymbol{k}_2, \boldsymbol{k}_3) \approx \frac{3}{2 + b_1(M)} Q^{(0)}_{\rm mmm}(\boldsymbol{k}_1, \boldsymbol{k}_2, \boldsymbol{k}_3) + \frac{b_2(M)}{2 b_1(M) + b_1^2(M)} \left[\frac{\widetilde{W}_{k_1, k_2} P^{(0)}_{\rm mm}(k_1) P^{(0)}_{\rm mm}(k_2) + 2\,{\rm cyc}}{P^{(0)}_{\rm mm}(k_1) P^{(0)}_{\rm mm}(k_2) + 2\,{\rm cyc}} \right]. \tag{B14}$$

Finally, in the limit that $k_i R \ll 1$, $\widetilde{W} \to 1$ and the above result can be approximated to

$$Q^{(0)}_{\rm hmm}(\boldsymbol{k}_1, \boldsymbol{k}_2, \boldsymbol{k}_3) \approx \frac{3}{2 + b_1(M)} Q^{(0)}_{\rm mmm}(\boldsymbol{k}_1, \boldsymbol{k}_2, \boldsymbol{k}_3) + \frac{b_2(M)}{2 b_1(M) + b_1^2(M)}. \tag{B15}$$

B2 Halo–halo–mass bispectrum in the local model

Again, using equation (B1), the halo–halo–mass bispectrum, symmetrized in the k_i arguments, can be written as

$$B_{\rm hhm}(\boldsymbol{k}_1, \boldsymbol{k}_2, \boldsymbol{k}_3) = b_1^2(M) B_{\rm mmm}(\boldsymbol{k}_1, \boldsymbol{k}_2, \boldsymbol{k}_3) + \frac{b_1(M) b_2(M)}{3} \int \frac{{\rm d}^3\boldsymbol{q}_1}{(2\pi)^3} \left[\widetilde{W}_{\boldsymbol{q}_1, \boldsymbol{k}_1 - \boldsymbol{q}_1} T_{\rm mmmm}(\boldsymbol{q}_1, \boldsymbol{k}_1 - \boldsymbol{q}_1, \boldsymbol{k}_2, \boldsymbol{k}_3) + 2\,{\rm cyc} \right]$$
$$+ \frac{b_2^2(M)}{12} \int \frac{{\rm d}^3\boldsymbol{q}_1}{(2\pi)^3} \frac{{\rm d}^3\boldsymbol{q}_2}{(2\pi)^3} \left[\widetilde{W}_{\boldsymbol{q}_1, \boldsymbol{k}_1 - \boldsymbol{q}_1} \widetilde{W}_{\boldsymbol{q}_2, \boldsymbol{k}_2 - \boldsymbol{q}_2} P_{5,{\rm m}}(\boldsymbol{q}_1, \boldsymbol{k}_1 - \boldsymbol{q}_1, \boldsymbol{q}_2, \boldsymbol{k}_2 - \boldsymbol{q}_2, \boldsymbol{k}_3) + 2\,{\rm cyc} \right]. \tag{B16}$$

If we use PT to expand P, B, T and P_5, and only keep terms that are of fourth order in the density field, then the above expression can be approximated to

$$B^{(0)}_{\rm hhm}(\boldsymbol{k}_1, \boldsymbol{k}_2, \boldsymbol{k}_3) \approx b_1^2(M) B^{(0)}_{\rm mmm}(\boldsymbol{k}_1, \boldsymbol{k}_2, \boldsymbol{k}_3) + \frac{1}{3} b_1(M) b_2(M) \left[\widetilde{W}_{k_1, k_2} P^{(0)}_{\rm mm}(k_1) P^{(0)}_{\rm mm}(k_2) + 2\,{\rm cyc} \right]. \tag{B17}$$

In the large-scale limit $k_i R \to 0$, the above expression can be approximated to

$$B^{(0)}_{\rm hhm}(\boldsymbol{k}_1, \boldsymbol{k}_2, \boldsymbol{k}_3) \approx b_1^2(M) B^{(0)}_{\rm mmm}(\boldsymbol{k}_1, \boldsymbol{k}_2, \boldsymbol{k}_3) + \frac{1}{3} b_1(M) b_2(M) \left[P^{(0)}_{\rm mm}(k_1) P^{(0)}_{\rm mm}(k_2) + 2\,{\rm cyc} \right]. \tag{B18}$$

The reduced bispectrum is given by

$$Q_{\rm hhm}(\boldsymbol{k}_1, \boldsymbol{k}_2, \boldsymbol{k}_3) \equiv \frac{B_{\rm hhm}(\boldsymbol{k}_1, \boldsymbol{k}_2, \boldsymbol{k}_3)}{P P_{\rm hhm}}, \tag{B19}$$

where

$$P P_{\rm hhm} = \frac{2}{3} \left[P_{\rm hh}(k_1) P_{\rm hm}(k_2) + 2\,{\rm cyc} \right] + \frac{1}{3} \left[P_{\rm hm}(k_1) P_{\rm hm}(k_2) + 2\,{\rm cyc} \right]. \tag{B20}$$

The halo–mass power spectrum is given by equation (B11) and the halo auto-power spectrum is given by

$$P_{\rm hh}(k) = b_1^2(M) P_{\rm mm}(\boldsymbol{k}_1) + b_1(M) b_2(M) \int \frac{{\rm d}^3\boldsymbol{q}_1}{(2\pi)^3} \widetilde{W}_{\boldsymbol{q}_1, \boldsymbol{k}_1 - \boldsymbol{q}_1} B_{\rm mmm}(\boldsymbol{q}_1, \boldsymbol{k}_1 - \boldsymbol{q}_1, -\boldsymbol{k}_1)$$
$$+ \frac{b_2^2(M)}{4} \int \frac{{\rm d}^3\boldsymbol{q}_1}{(2\pi)^3} \frac{{\rm d}^3\boldsymbol{q}_2}{(2\pi)^3} \widetilde{W}_{\boldsymbol{q}_1, \boldsymbol{k}_1 - \boldsymbol{q}_1} \widetilde{W}_{\boldsymbol{q}_2, -\boldsymbol{k}_1 - \boldsymbol{q}_2} T_{\rm mmmm}(\boldsymbol{q}_1, \boldsymbol{k}_1 - \boldsymbol{q}_1, \boldsymbol{q}_2, -\boldsymbol{k}_1 - \boldsymbol{q}_2). \tag{B21}$$

Expanding the above expression to lowest order in PT gives

$$P P^{(0)}_{\rm hhm} \approx \frac{2 b_1^2(M)}{3} \left[2 b_1(M) + 1 \right] \left[P^{(0)}_{\rm mm}(k_1) P^{(0)}_{\rm mm}(k_2) + 2\,{\rm cyc} \right]. \tag{B22}$$

Using the above expression, we find that the tree-level expression for the reduced bispectrum can be written as

$$Q^{(0)}_{\rm hhm}(\boldsymbol{k}_1, \boldsymbol{k}_2, \boldsymbol{k}_3) \approx \frac{3}{2 b_1(M) + 1} Q^{(0)}_{\rm mmm}(\boldsymbol{k}_1, \boldsymbol{k}_2, \boldsymbol{k}_3) + \frac{2 b_2(M)}{2 b_1^2(M) + b_1(M)} \left[\frac{\widetilde{W}_{k_1, k_2} P^{(0)}_{\rm mm}(k_1) P^{(0)}_{\rm mm}(k_2) + 2\,{\rm cyc}}{P^{(0)}_{\rm mm}(k_1) P^{(0)}_{\rm mm}(k_2) + 2\,{\rm cyc}} \right]. \tag{B23}$$

In the large-scale limit $k_i R \to 0$, we again have $\widetilde{W} \to 1$ and

$$Q^{(0)}_{\rm hhm}(\boldsymbol{k}_1, \boldsymbol{k}_2, \boldsymbol{k}_3) \approx \frac{3}{2 b_1(M) + 1} Q^{(0)}_{\rm mmm}(\boldsymbol{k}_1, \boldsymbol{k}_2, \boldsymbol{k}_3) + \frac{2 b_2(M)}{2 b_1^2(M) + b_1(M)}. \tag{B24}$$

B3 Halo–halo–halo bispectrum in the local model

Again using equation (B1), the halo–halo–halo bispectrum, symmetrized in the k_i arguments, can be written as

$$B_{\rm hhh}(\boldsymbol{k}_1,\boldsymbol{k}_2,\boldsymbol{k}_3) = b_1^3(M)B_{\rm mmm}(\boldsymbol{k}_1,\boldsymbol{k}_2,\boldsymbol{k}_3) + \frac{1}{2}b_1^2(M)b_2(M)\int\frac{{\rm d}^3\boldsymbol{q}_1}{(2\pi)^3}\left[\widetilde{W}_{\boldsymbol{q}_1,\boldsymbol{k}_1-\boldsymbol{q}_1}T_{\rm mmmm}(\boldsymbol{q}_1,\boldsymbol{k}_1-\boldsymbol{q}_1,\boldsymbol{k}_2,\boldsymbol{k}_3)+2\,{\rm cyc}\right]$$
$$+\frac{1}{4}b_1b_2^2\int\frac{{\rm d}^3\boldsymbol{q}_1}{(2\pi)^3}\frac{{\rm d}^3\boldsymbol{q}_2}{(2\pi)^3}\left[\widetilde{W}_{\boldsymbol{q}_1,\boldsymbol{k}_1-\boldsymbol{q}_1}\widetilde{W}_{\boldsymbol{q}_2,\boldsymbol{k}_2-\boldsymbol{q}_2}P_{5,{\rm m}}(\boldsymbol{q}_1,\boldsymbol{k}_1-\boldsymbol{q}_1,\boldsymbol{q}_2,\boldsymbol{k}_2-\boldsymbol{q}_2,\boldsymbol{k}_3)+2\,{\rm cyc}\right]$$
$$+\frac{b_2^3}{8}\int\frac{{\rm d}^3\boldsymbol{q}_1}{(2\pi)^3}\frac{{\rm d}^3\boldsymbol{q}_2}{(2\pi)^3}\frac{{\rm d}^3\boldsymbol{q}_3}{(2\pi)^3}\widetilde{W}_{\boldsymbol{q}_1,\boldsymbol{k}_1-\boldsymbol{q}_1}\widetilde{W}_{\boldsymbol{q}_2,\boldsymbol{k}_2-\boldsymbol{q}_2}\widetilde{W}_{\boldsymbol{q}_3,\boldsymbol{k}_3-\boldsymbol{q}_3}P_{6,{\rm m}}(\boldsymbol{q}_1,\boldsymbol{k}_1-\boldsymbol{q}_1,\boldsymbol{q}_2,\boldsymbol{k}_2-\boldsymbol{q}_2,\boldsymbol{q}_3,\boldsymbol{k}_3-\boldsymbol{q}_3). \quad ({\rm B25})$$

If we use PT to expand P, B, T, P_5 and P_6, and keep only terms that are of fourth order in the density field, then the above expression can be approximated to

$$B^{(0)}_{\rm hhh}(\boldsymbol{k}_1,\boldsymbol{k}_2,\boldsymbol{k}_3) \approx b_1^3(M)B^{(0)}_{\rm mmm}(\boldsymbol{k}_1,\boldsymbol{k}_2,\boldsymbol{k}_3) + b_1^2(M)b_2(M)\left[\widetilde{W}_{\boldsymbol{k}_1,\boldsymbol{k}_2}P^{(0)}_{\rm mm}(k_1)P^{(0)}_{\rm mm}(k_2)+2\,{\rm cyc}\right]. \quad ({\rm B26})$$

In the large-scale limit $k_iR \to 0$, the above expression can be approximated to

$$B^{(0)}_{\rm hhh}(\boldsymbol{k}_1,\boldsymbol{k}_2,\boldsymbol{k}_3) \approx b_1^3(M)B^{(0)}_{\rm mm}(\boldsymbol{k}_1,\boldsymbol{k}_2,\boldsymbol{k}_3) + b_1^2(M)b_2(M)\left[P^{(0)}_{\rm mm}(k_1)P^{(0)}_{\rm mm}(k_2)+2\,{\rm cyc}\right]. \quad ({\rm B27})$$

The reduced halo–halo–halo bispectrum is given by

$$Q_{\rm hhh}(\boldsymbol{k}_1,\boldsymbol{k}_2,\boldsymbol{k}_3) \equiv \frac{B_{\rm hhh}(\boldsymbol{k}_1,\boldsymbol{k}_2,\boldsymbol{k}_3)}{P\,P_{\rm hhh}}, \quad ({\rm B28})$$

where

$$P\,P_{\rm hhh} = \left[P_{\rm hh}(k_1)P_{\rm hh}(k_2)+2\,{\rm cyc}\right], \quad ({\rm B29})$$

where the halo auto-power spectrum is given by equation (B21). On expanding the above expression to fourth order in the density, we find

$$P\,P^{(0)}_{\rm hhh} \approx b_1^4(M)\left[P^{(0)}_{\rm mm}(k_1)P^{(0)}_{\rm mm}(k_2)+\,2\,{\rm cyc}\right]. \quad ({\rm B30})$$

Using the above expression, we find that the tree-level expression for the reduced bispectrum can be written as

$$Q^{(0)}_{\rm hhh}(\boldsymbol{k}_1,\boldsymbol{k}_2,\boldsymbol{k}_3) \approx \frac{1}{b_1(M)}Q^{(0)}_{\rm mmm}(\boldsymbol{k}_1,\boldsymbol{k}_2,\boldsymbol{k}_3) + \frac{b_2(M)}{b_1^2(M)}\left[\frac{\widetilde{W}_{k_1,k_2}P^{(0)}_{\rm mm}(k_1)P^{(0)}_{\rm mm}(k_2)+2\,{\rm cyc}}{P^{(0)}_{\rm mm}(k_1)P^{(0)}_{\rm mm}(k_2)+2\,{\rm cyc}}\right]. \quad ({\rm B31})$$

In the large-scale limit $k_iR \to 0$, we again have $\widetilde{W} \to 1$ and

$$Q^{(0)}_{\rm hhh}(\boldsymbol{k}_1,\boldsymbol{k}_2,\boldsymbol{k}_3) \approx \frac{1}{b_1(M)}Q^{(0)}_{\rm mmm}(\boldsymbol{k}_1,\boldsymbol{k}_2,\boldsymbol{k}_3) + \frac{b_2(M)}{b_1^2(M)}. \quad ({\rm B32})$$

This paper has been typeset from a TEX/LATEX file prepared by the author.